1
Polymer Dynamics in Melts

Andreas Wischnewski and Dieter Richter

Abstract

The dynamics of linear polymer chains in the melt depends strongly on the chain length: for short, unentangled chains, the dynamics is determined by a balance of viscous and entropic forces; for long chains, topological constraints are dominant. In this chapter, the experimental exploration of chain dynamics is introduced and discussed in detail. The focus is on neutron spin-echo (NSE) spectroscopy, which is one of the most powerful tools to explore the different dynamic regimes in polymer melts on a microscopic scale. It allows direct observation of the transition from a regime of free relaxation at short times, which can be described in terms of the Rouse model, to constrained motion at longer times. The constrained motion is caused by the entanglements that emerge in long-chain polymer systems. The tube concept models these topological confinements by assuming the chain to be confined in a virtual tube formed by adjacent chains. This concept of chains reptating in a tube is strongly supported by experiments in the limit of long chains.

However, there is also strong experimental evidence that the tube model starts to fail if the polymer chains become shorter. In this regime of intermediate chain length, neither the Rouse model nor the pure reptation concept are applicable. A close comparison of linear rheology data with the predictions of the reptation model indicates the existence of additional degrees of freedom that release the topological confinement. Fluctuating chain ends that destroy the tube confinement starting from both ends were proposed as one candidate. This process, called contour length fluctuations (CLF), indeed accounts for the observed behavior of the mechanical relaxation function. In this chapter, we present a systematic study of this mechanism on a microscopic scale.

A second relaxation process that appears to limit the topological confinement in polymer melts is the relaxation of the tube itself (constraint release). Since the tube is formed by adjacent chains, which themselves accomplish all motions that are permitted for an observed test chain, the topological constraints that are represented by the tube are not fixed in time. In this chapter, the loosening of confinement by the constraint release effect, which can be observed on a molecular scale, will be investigated.

1.1
Introduction

In this chapter, the dynamics of flexible polymers in the melt – one of the most fascinating topics in the field of polymer science – will be discussed. The structure of polymer chains has been the subject of intensive scientific work at both theoretical and experimental levels, so it is a logical consequence of the activity in that field to focus on the problem of how these large molecules move. This question becomes all the more challenging because the static properties alone are surprising. Drawing the structural formula of a polymer on paper, one could be tempted to conclude that the chains in reality are prolate objects. The fundamental investigation of Flory (1953) has shown that this is not the case. His prediction that the spatial extent of a large chain molecule should be coil-like rather than rod-like (stretched) was confirmed by neutron scattering experiments (Kirste et al. 1973). This was at the same time one of the first applications of neutron scattering to polymer science. The coil conformation is a consequence of the large number of internal degrees of freedom, a common property of soft matter systems. Further "soft matter properties" of polymers are the weak interaction between the structural units (chains) and the significant role of entropy.

The mechanical properties of polymers are extraordinarily diverse. Addressing the response to strain, condensed matter is generally divided into solids and liquids: for solids, the stress is proportional to the strain at least for small deformations (elastic behavior); for liquids, the stress is proportional to the change in strain, i.e. viscous behavior is observed. For a polymer, the mechanical response can be solid-like, rubber-like or viscous depending on the temperature or load time. For long-chain polymer melts at intermediate frequencies, a plateau in the relaxation function reflects elastic behavior. In the low-frequency region, i.e. at longer times, the same material behaves in a viscous manner. This "viscoelastic" behavior is a good reason for comparing a long-chain polymer melt with a network, where chains are chemically cross-linked. In a melt, there are no chemical cross-links; however, if the chains are long enough, they build entanglements, which are not stable but may act

temporarily as network points. In this picture, the plateau in the relaxation function is caused by a temporary network and, in analogy to the mesh size in a real network, one can define a distance between the entanglements in the melt: typical distances are in the order of some nanometers. Compared with the segment length (around 0.5 nm) and the radius of the coil of the entire chain (around 100 nm), this distance defines an intermediate length scale.

We have seen that the dynamics of polymers strongly depend on the time scales and temperature under consideration. One may also focus on different length scales. If a polymer is subjected to a mechanical strain, complex molecular rearrangements are provoked. This relates not only to molecular dimensions but also to individual bonds. Since local bond dynamics is governed by local potentials, the rearrangements are comparably fast to a normal solid (picosecond range). For distances between the bond length and the entanglement distance, entropic forces are dominant. For even larger distances, the motion of the chain is restricted due to the entanglements, and the chain is localized. All these dynamic processes, starting from lengths of about 0.1 nm and times in the picosecond range up to the size of the polymer chain (about 100 nm) and up to macroscopic times, determine the viscoelastic properties of a polymer system.

Thus, the dynamics of polymers is manifold: the relevant length scales vary from atomic distances to the length of the polymer macromolecule. This leads to time scales that are comparable to the characteristic time scales of atomic vibrations up to very long "macroscopic" times. The wide range of relevant time and length scales for polymers leads to their various mechanical properties. The huge variety of applications in conjunction with their simple production and processing makes polymers particular and interesting. Polymers are an integral part of our daily lives and they are of utmost importance for industry.

It is evident that a discussion of polymer dynamics over the entire range of time scales is far beyond the scope of this chapter. Here, we will focus on polymers at high temperatures, far beyond the glass temperature T_g, where a polymer is in the liquid-like "melt state". Furthermore, we will not discuss the local dynamics or glass aspects, but concentrate on the mesoscopic dynamics, i.e. on intermediate to large length scales that are in the order of the entire polymer chain, or some units of it. The manifold dynamic behavior on mesoscopic length scales is completely unknown from conventional solid-state physics. Consequently, specific experimental techniques and theoretical approaches are required. For instance, if a macromolecule that "prefers" the coil conformation is stretched a little bit – say by Brownian motion of neighboring molecules – the entropy will try to bend it back. On the other hand, the molecule has to overcome friction if it wants to move. How can this behavior be described? Another aspect to address is the question of how these large

molecules diffuse and on what time scale. As mentioned above, long polymer chains will build entanglements, or packing constraints will strongly affect the freedom to move. What kind of chain motion will this condition allow?

One fascinating property of polymers on large length scales is universality. The principles we are going to discuss in this chapter do not depend on local, chemical details. This leads to the fact that we can focus our studies on one or two polymers to elucidate the main features of dynamical behavior.

One ultimate goal of polymer science is an understanding of macroscopic dynamic and mechanical properties on a molecular basis. The hope is that revealing all dynamic processes in polymer systems not only gives an essential contribution to fundamental research but also allows the design of materials with specific macroscopic properties by selectively manipulating microscopic parameters like architecture or composition. This "molecular design" presumes an understanding of all relevant relaxation processes in polymers, and we hope that the following pages serve as a first step in this direction.

In Section 1.2 the basic properties of polymer chains are discussed. Here, a brief introduction to the synthesis of polymer chains and their characterization is also given. In Section 1.3, experimental techniques that allow one to access the mechanical and dynamic properties will be introduced. Sections 1.4 to 1.6 describe theoretical approaches that are available and can explain the main features of polymer melt systems, starting from the Brownian dynamics of a single segment of a polymer chain to the large-scale diffusion of an entire macromolecule. These concepts will be scrutinized by experiments. The results demand the consideration of secondary relaxation processes, which will be discussed and again tested by experiments in Sections 1.7 and 1.8. Finally, in Section 1.9 the chapter will be summarized and an outlook will be given.

1.2
What is a Polymer?

Polymers are large molecules that are built from a repeat unit, the monomer. If all monomers are of the same species, the polymer is called a homopolymer. If a chain consists of several parts (blocks) that are chemically different, they are denoted as diblock or multiblock copolymers. The segments may be linked one after another, which leads to linear chains, or, by introducing branching points, versatile complex architectures can be produced. In polymer science, star polymers with different numbers of "arms" (one branching point), structures with one backbone chain and two (H-shaped) or more (pom-poms) arms at each end (two branching points), and even more complex molecules with a
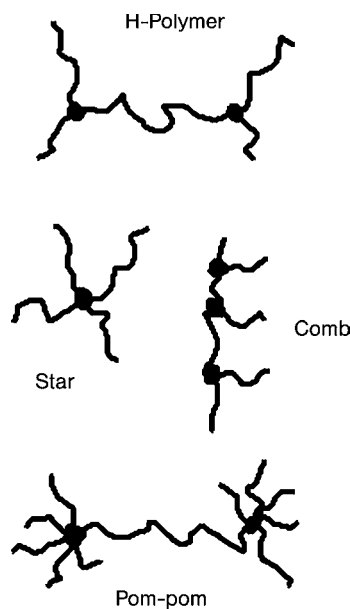
H-Polymer

Comb

Star

Pom-pom

Fig. 1.1 Schematic representation of different polymer architectures.

comb-like structure have been considered and intensively investigated in the past decades (see Fig. 1.1).

In addition to the variation of the chemical structure within one chain or the architecture of the molecules, interesting features are found in mixed systems, e.g. in polymer blends that consist of different homopolymers, chains with different length (polydisperse systems) or architecture. Also, polymer solutions should be mentioned here.

Converging to an understanding of the basic dynamic properties in polymers presumes an understanding of the simplest systems. Therefore, we will focus in this chapter on homopolymers with a linear architecture in the melt state. They are the ideal probe to investigate the motions on the scale of segments and chains, respectively. In the following sections, we will see that the main features of polymer dynamics strongly depend on the length of the chains or the number of monomers N, respectively.

1.2.1
Synthesis of Polymers

Modern polymer chemistry generally distinguishes between two basic polymerization mechanisms (Odian 1991). These are either step growth or chain growth polymerizations. Step growth polymerization proceeds by the step-

wise reaction between the functional groups of reactants, which can be either monomers, oligomers or polymers. In such polymerizations, the size of the polymer increases at a relatively slow rate and reaches a high molecular weight only if high conversion is reached. Typical examples for step growth polymerizations are the formation of polyamides by the reaction of diamines with dicarboxylic acids or the formation of polyurethanes by reaction of diisocyanates with diols. In contrast to step growth, chain growth polymerizations require an initiator. The initiator produces a reactive center, which may be either a free radical, cation, or anion. The monomer reacts exclusively with the reactive center and not with other monomers, oligomers or polymers. Chain growth polymerization can be subdivided into four elementary steps, i.e. initiation, propagation, chain transfer, and termination.

- During the initiation step, a reactive center, I^*, is formed, which initiates chain growth by reaction with the monomer M:

$$I \longrightarrow I^*$$

$$I^* + M \longrightarrow I\text{--}M^*$$
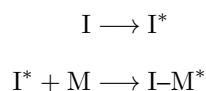
- During propagation, the reactive species repeatedly reacts with the monomer:

$$I\text{--}M^* + nM \longrightarrow I\text{--}(M)_n\text{--}M^*$$
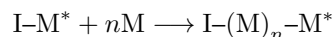
where n denotes the number of monomers incorporated into the growing chain and $n + 1 = N$ is the degree of polymerization (number of monomers of the terminated chain).

- Termination is the step where the reactive center is destroyed by reaction with a compound S. At this point, the polymer chain, P, is inactive and ceases to grow:

$$I\text{--}(M)_n\text{--}M^* + S \longrightarrow P$$
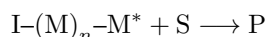
- An additional reaction step that has to be considered is chain transfer. This step involves reaction with a compound S–X leading to a terminated polymer chain P–X, but at the same time to a new reactive species S^*, which itself acts as an initiator for chain growth:

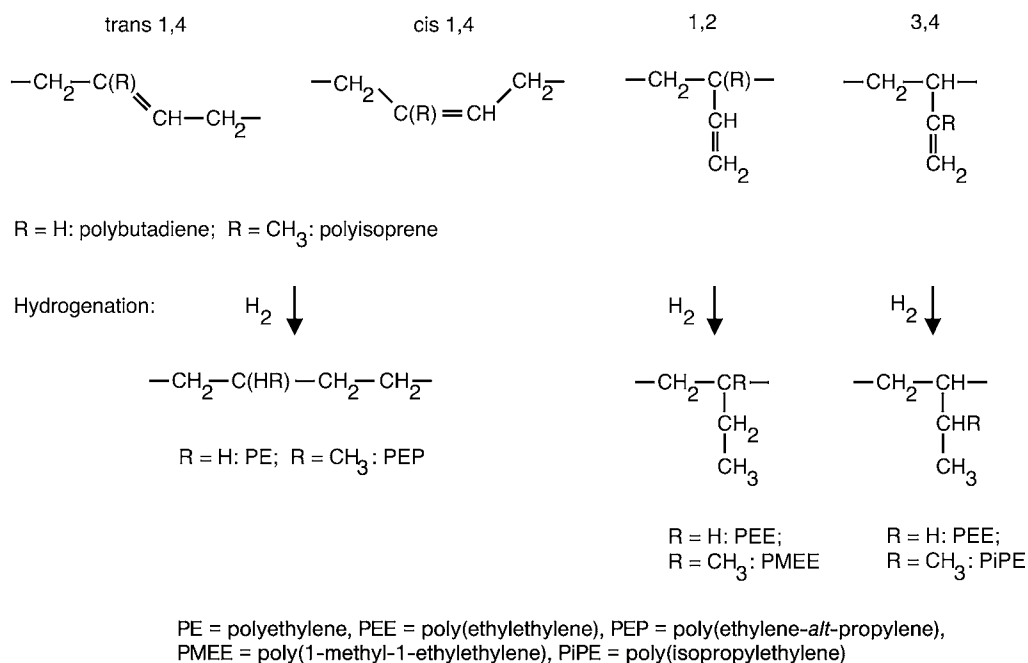$$I\text{--}(M)_n\text{--}M^* + S\text{--}X \longrightarrow P\text{--}X + S^*$$
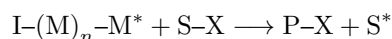
A special case of chain growth polymerization is obtained when termination and chain transfer can be suppressed. This process is called *living*

polymerization, which in particular is essential for the preparation of model polymers as outlined in the following paragraph. A detailed description of the definitions of, criteria for and consequences of living polymerizations can be found in the literature (Hsieh and Quirk 1996; Matyjaszewski and Sawamoto 1996; Kamigaito et al. 2001).

Under living polymerization conditions it is possible to synthesize model polymers with well-defined composition and structure, e.g. block copolymers by consecutive polymerization of two or more monomers, or star polymers by reaction with an appropriate coupling agent. The molecular weight of the polymers can be anticipated simply by the ratio of the mass of monomer to the moles of initiator provided that 100% conversion is reached. Polymers with narrow molecular-weight distribution can be prepared if the initiation rate is fast or comparable to the propagation rate and a rapid mixing of the reactants is ensured. Hence, polymerizations accomplished under such conditions yield model polymers suitable in particular for fundamental research in polymer physics. In this respect anionic polymerization of styrene and dienes with alkyllithium initiators has turned out to be the most powerful method (Young et al. 1984), even though living cationic and living radical polymerization have become increasingly important in recent years. In the following we will focus on the preparation and properties of some polyolefins, which are of particular importance for this chapter.

Polyolefins are saturated hydrocarbon polymers that exhibit superior stability toward thermal, oxidative, and radiation-induced degradation. They are therefore suitable for fundamental studies under extreme conditions, e.g. in the high-T limit. Polyolefins can be prepared by Ziegler–Natta and metallocene catalysts or by free-radical polymerization. Unfortunately, the polymers prepared by these methods usually possess a relatively broad polydispersity and the molecular architecture is difficult to control. In order to produce model polyolefins with narrow molecular-weight distribution, predefined molecular weights, and controlled architecture, the synthetic strategy involves the preparation of polydienes by living anionic polymerization, which are subsequently saturated with hydrogen to the corresponding polyolefins, e.g. polyethylene (PE) and poly(ethylene-*alt*-propylene) (PEP) can be made from polybutadiene and polyisoprene, respectively (see Fig. 1.2). Such polymerized polyolefins differ from pure linear chains by the appearance of a certain amount of side chains. This is due to the microstructure of the parent polydienes, which consists of four modes: *cis*-1,4-, and *trans*-1,4-, 1,2- and 3,4-. Polymerization of 1,3-butadiene in hydrocarbon solvents (benzene, cyclohexane) with alkyllithium initiator concentrations below 10^{-2} mol l^{-1} leads to a microstructure of about 51% *trans*-1,4-, 42% *cis*-1,4- and 7% 1,2- addition. The 1,2- and 3,4- isomers are identical in polybutadiene.

trans 1,4   cis 1,4   1,2   3,4

$-CH_2-C(R)$
$\quad\quad\quad CH-CH_2-$

$-CH_2$
$\quad\quad C(R)=CH$
$\quad\quad\quad\quad\quad CH_2-$

$-CH_2-C(R)-$
$\quad\quad\quad CH$
$\quad\quad\quad \|$
$\quad\quad\quad CH_2$

$-CH_2-CH-$
$\quad\quad\quad CR$
$\quad\quad\quad \|$
$\quad\quad\quad CH_2$

R = H: polybutadiene; R = CH_3: polyisoprene

Hydrogenation: H_2 ↓ H_2 ↓ H_2 ↓

$-CH_2-C(HR)-CH_2-CH_2-$

R = H: PE; R = CH_3: PEP

$-CH_2-CR-$
$\quad\quad\quad CH_2$
$\quad\quad\quad |$
$\quad\quad\quad CH_3$

$-CH_2-CH-$
$\quad\quad\quad CHR$
$\quad\quad\quad |$
$\quad\quad\quad CH_3$

R = H: PEE;
R = CH_3: PMEE

R = H: PEE;
R = CH_3: PiPE

PE = polyethylene, PEE = poly(ethylethylene), PEP = poly(ethylene-*alt*-propylene),
PMEE = poly(1-methyl-1-ethylethylene), PiPE = poly(isopropylethylene)

Fig. 1.2 Schematic illustration of possible microstructures of polyiso-
prene and polybutadiene and their transformation to the respective
polyolefins by hydrogenation.

The microstructure of polyisoprene prepared under similar conditions con-
sists of about 70% *cis*-1,4-, 23% *trans*-1,4- and 7% 3,4- units. The 1,2- addi-
tion does not appear in hydrocarbons. The composition of the microstructure
changes drastically when polymerizations are performed in polar solvents like
tetrahydrofuran or diethyl ether. The *cis*-1,4- and *trans*-1,4- units are clearly
reduced, while beside an increased amount of 3,4- also 1,2- units are ob-
tained. In the case of polybutadiene, the presence of 1,2- addition can be
driven to almost 100% with dipiperidinoethane as polar cosolvent in a molar
excess of at least 4 over the initiator. The polydienes can be saturated in a
post-polymerization reaction by addition of hydrogen to the corresponding
polyolefins. Several homogeneous and heterogeneous catalytic methods have
been applied to get polyolefins with the same molecular characteristics as the
parent polydienes. It turns out that heterogeneous catalytic hydrogenation by
means of a palladium/barium sulfate catalyst is the most effective for this
requirement. In particular, for the hydrogenation of polybutadienes and poly-
isoprenes, no chain scission and complete saturation are observed. There is
also no metal contamination due to the ease of catalyst extraction.

The amount and type of side chains in the polyolefins prepared via this route obviously depend on the microstructure of the polydiene precursors. The hydrogenation product from *cis*-1,4- and *trans*-1,4-polyisoprene is an alternating poly(ethylene–propylene) (PEP) copolymer, the 1,2- structure transforms into poly(1-methyl-1-ethylethylene) (PMEE) and the 3,4- structure into poly(isopropylethylene) (PiPE). Hence, the hydrogenation product from polyisoprene prepared in a hydrocarbon solvent is in fact an alternating copolymer of ethylene and propylene with a random distribution of 7% isopropylethylene units. However, the abbreviation PEP has been accepted for this material and will be also used in this chapter.

A similar but less complicated scenario is obtained for polybutadiene. The *cis*-1,4- and *trans*-1,4- structures yield linear polyethylene (PE), and the 1,2- structure poly(ethylethylene) (PEE). PEE is formally the polymerization product of 1-butene. Therefore, the hydrogenation product of polybutadiene is a random copolymer of ethylene and 1-butene. The widely accepted abbreviation for this polymer is PEB-x [poly(ethylene-*co*-butene)-x], where the integer x denotes the number of ethyl side branches per 100 backbone carbons. According to this nomenclature, the hydrogenation product of a polybutadiene with 93% 1,4- and 7% 1,2- units is PEB-2 and that of 100% 1,2- polybutadiene is PEB-50.

Due to the presence of side chains, the average molar mass of a repeat unit M_0 is calculated as typically shown for PEB-2 in the following: If we cut from a long PEB-2 polymer chain a subchain with 100 carbon atoms ($M = 1200 \, \text{g mol}^{-1}$), it has $200 - 2 = 198$ hydrogen atoms ($M = 198 \, \text{g mol}^{-1}$) and two ethyl branches C_2H_5 ($M = 58 \text{ g mol}^{-1}$), which yields a molecular weight of 1456 g mol^{-1}, i.e. $M_0 \approx 14.6$ g mol^{-1}. In analogy to PEP and for the sake of clarity, we use PE for PEB-2 and PEE for PEB-50 throughout this chapter.

1.3
Experimental Techniques

1.3.1
Neutron Scattering

Neutron scattering (Squires 1978) is a powerful tool for the investigation of the structure and dynamics in condensed matter samples at atomic and intermediate scales. Neutrons may be produced by a nuclear chain reaction in a reactor. They are moderated by, for example, D_2O before they react with the next nucleus. To produce slow ("cold") neutrons, a cold source is inserted into the reactor, which moderates the thermal neutrons to low temperatures

(e.g. by hydrogen with a temperature of 20 K). An alternative method for the production of neutrons is spallation, where a high-energy beam of hydrogen ions hits a heavy-metal target so that neutrons evaporate from the cores. For a pulsed operation of the ion accelerator, a broad band of wavelengths may be used for the scattering experiments.

Thermal and cold neutrons have de Broglie wavelengths from $\lambda = 0.1$ nm up to 2 nm, corresponding to typical distances in condensed matter systems. The kinetic energy of the neutrons compares with the excitation energies of atomic or molecular motions like vibrations or phonons. Therefore, motions of the scatterers in condensed matter samples are detectable by a velocity change of the neutron. The spatial character of the motion may be inferred from the angular distribution of the scattered neutrons. The fact that neutrons deliver information about the structure and the dynamics at the same time makes them one of the most important tools in condensed matter research.

The energy E and momentum p of a neutron can be defined by the velocity v (here, the neutron is seen as a particle) or the wavenumber $k = 2\pi/\lambda$ (here, the neutron is seen as a wave with wavelength λ):

$$\boldsymbol{p} = m_\mathrm{n}\boldsymbol{v} = \hbar\boldsymbol{k} \tag{1.1}$$

$$E = \frac{m_\mathrm{n}}{2}v^2 = \frac{(\hbar k)^2}{2m_\mathrm{n}} \tag{1.2}$$

where m_n is the mass of the neutron. Fig. 1.3 shows the principle of a scattering experiment. A neutron beam of intensity I_0 with neutrons of energy E_i and a wavevector $\boldsymbol{k}_\mathrm{i}$ is scattered at the sample. The interaction of the neutron with the sample can be divided into two types. The first type is the magnetic interaction, where the magnetic moment of the neutron interacts with the
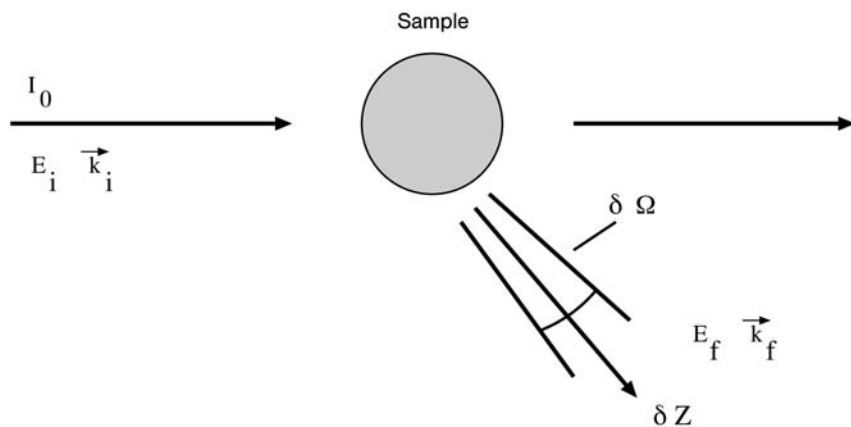

Fig. 1.3 Principle of a scattering experiment.

magnetic moment of the electrons or the cores. This type of interaction has no relevance for the topic discussed here, so we will focus on the second type, the scattering of the neutron at the core potential by the strong interaction. The strength of this interaction is represented by the scattering length b_j, a complex number that varies with the mass number of the core in an unsystematic way. The real part of b_j represents the scattering, and the imaginary part the absorption of the neutrons.

In the solid angle $\delta\Omega$ steradians, the scattered neutrons δZ can be characterized by energy E_f and wavevector $\boldsymbol{k}_\mathrm{f}$. The energy and momentum that were transferred by the scattering process is given by

$$\Delta E = \hbar\omega = E_\mathrm{i} - E_\mathrm{f} \tag{1.3}$$

$$\Delta\boldsymbol{p} = \hbar\boldsymbol{Q} = \hbar(\boldsymbol{k}_\mathrm{i} - \boldsymbol{k}_\mathrm{f}) \tag{1.4}$$

where $\boldsymbol{Q}$ is the scattering vector. If $E_\mathrm{i} = E_\mathrm{f}$, the scattering process is called elastic. Following Eq. (1.2), this also means that $k_\mathrm{i} = |\boldsymbol{k}_\mathrm{i}| = k_\mathrm{f} = |\boldsymbol{k}_\mathrm{f}| = 2\pi/\lambda$.

We have to distinguish between coherent and incoherent scattering. The nucleus as well as the isotope distribution determine how much of these fractions contribute to the scattering. For elements that have a nucleus with spin zero and only one isotope, the scattering is purely coherent, i.e. the scattering of different atoms interferes. If the spin is not zero, the scattering amplitude may depend on the relative orientation of the nuclear and neutron spins, respectively. Then we are dealing with a mean scattering amplitude, which contains a coherent part and fluctuations of the scattering amplitude that contribute to the intensity without interference of waves emitted from different atoms. The latter represents the behavior of single atoms and is called incoherent. For vanadium or hydrogen, for example, incoherent scattering is significantly stronger than coherent scattering.

Let us describe coherent scattering of an atom by the mean scattering length squared $\bar{b}^2$ and incoherent scattering by the scattering cross-section $\sigma_\mathrm{inc} = 4\pi(\overline{b^2} - \bar{b}^2)$. The coherent part of the double differential cross-section of N equal atoms is given by (Marshall and Lovesey 1971)

$$\left(\frac{\mathrm{d}^2\sigma}{\mathrm{d}\omega\,\mathrm{d}\Omega}\right)_\mathrm{coh} = \frac{k_\mathrm{f}}{k_\mathrm{i}}\frac{1}{2\pi}\int_{-\infty}^{\infty}\mathrm{d}t\,\mathrm{e}^{-\mathrm{i}\omega t}\,\bar{b}^2\sum_{i,j=1}^{N}\left\langle\mathrm{e}^{-\mathrm{i}\boldsymbol{Q}\boldsymbol{R}_i(0)}\mathrm{e}^{\mathrm{i}\boldsymbol{Q}\boldsymbol{R}_j(t)}\right\rangle \tag{1.5}$$

The angle brackets denote an ensemble average. The incoherent part of the double differential cross-section is given by

$$\left(\frac{\mathrm{d}^2\sigma}{\mathrm{d}\omega\,\mathrm{d}\Omega}\right)_\mathrm{inc} = \frac{k_\mathrm{f}}{k_\mathrm{i}}\frac{1}{2\pi}\int_{-\infty}^{\infty}\mathrm{d}t\,\mathrm{e}^{-\mathrm{i}\omega t}\,\frac{\sigma_\mathrm{inc}}{4\pi}\sum_{i=1}^{N}\left\langle\mathrm{e}^{-\mathrm{i}\boldsymbol{Q}\boldsymbol{R}_i(0)}\mathrm{e}^{\mathrm{i}\boldsymbol{Q}\boldsymbol{R}_i(t)}\right\rangle \tag{1.6}$$

Now we can express the cross-sections by a normalized dynamic structure factor $S(\boldsymbol{Q}, \omega)$:

$$S_{\text{coh}}(\boldsymbol{Q}, \omega) = \frac{k_{\text{i}}}{k_{\text{f}}} \frac{1}{N\overline{b}^2} \left(\frac{\mathrm{d}^2\sigma}{\mathrm{d}\omega\,\mathrm{d}\Omega} \right)_{\text{coh}} \tag{1.7}$$

The polymer systems that will be discussed in this chapter are isotropic without any preferential direction. Thus, we may use

$$S_{\text{coh}}(Q, \omega) = S_{\text{coh}}(\boldsymbol{Q}, \omega) \tag{1.8}$$

For incoherent scattering $S_{\text{inc}}(Q, \omega)$ is

$$S_{\text{inc}}(Q, \omega) = \frac{k_{\text{i}}}{k_{\text{f}}} \frac{4\pi}{N\sigma_{\text{inc}}} \left(\frac{\mathrm{d}^2\sigma}{\mathrm{d}\omega\,\mathrm{d}\Omega} \right)_{\text{inc}} \tag{1.9}$$

It can be shown that the coherent dynamic structure factor is the Fourier transform (with respect to space and time) of the van Hove pair correlation function $G_{\text{pair}}(R, t)$ (van Hove 1954). In a classical interpretation this function stands for the probability of finding an atom j at position R_j at time t, if any atom i has been at position $R_i = 0$ at time $t = 0$. In analogy to the pair correlation function, the self-correlation function $G_{\text{self}}(R, t)$ is obtained by a Fourier transform of the incoherent scattering factor. Then $G_{\text{self}}(R, t)$ represents the probability of finding the atom i at position R_i at time t if the same atom has been at $R_i = 0$ at time $t = 0$.

Finally, before discussing two important neutron scattering techniques, which are vital for the understanding of the dynamics in polymer systems, we define the elastic scattering function as $S(Q, 0) \equiv S(Q, \omega{=}0)$ and the static scattering function $S(Q)$, which is directly measured by small-angle neutron scattering (SANS):

$$S(Q) \equiv S(Q, t{=}0) = \int_{-\infty}^{\infty} S(Q, \omega)\,\mathrm{d}\omega \tag{1.10}$$

As we will see below, in the neutron spin-echo technique, the Fourier transform of $S(Q, \omega)$ can be measured directly. The coherent scattering function in the time domain, also called the intermediate scattering function, can be calculated by the Fourier transform of Eq. (1.7) and using Eq. (1.8):

$$S_{\text{coh}}(Q, t) = \frac{1}{N} \sum_{i,j=1}^{N} \left\langle e^{-i\boldsymbol{Q}\boldsymbol{R}_i(0)} e^{i\boldsymbol{Q}\boldsymbol{R}_j(t)} \right\rangle \tag{1.11}$$

The respective incoherent scattering function is given by the Fourier transform of Eq. (1.9):

$$S_{\text{inc}}(Q, t) = \frac{1}{N} \sum_{i=1}^{N} \left\langle e^{-i\boldsymbol{Q}\boldsymbol{R}_i(0)} e^{i\boldsymbol{Q}\boldsymbol{R}_i(t)} \right\rangle \qquad (1.12)$$

Small-Angle Neutron Scattering (SANS)

At a given wavelength of the probing radiation, large objects scatter into small angles. Long polymer chains are much larger than single atoms – their size is mesoscopic. To obtain information on the chain conformation, small scattering angles and therefore small Q-values have to be resolved. This can be realized by small-angle neutron scattering (SANS). In this technique, no energy analysis of the scattered neutrons is performed; the integral over all energies is detected. The measured scattering function $S(Q)$ therefore contains information about the structure of the sample but not about the dynamics.

The schematic picture of the experimental setup is shown in Fig. 1.4. A polychromatic neutron beam from a cold moderator is monochromated by a neutron velocity selector. This is a rotating cylinder with tilted absorbing lamellas. Only neutrons with a defined wavelength λ ($\Delta\lambda/\lambda \approx 0.1$) can pass. Neutron guides bring the neutrons to the collimation aperture. Then, the neutrons propagate freely to the sample aperture, which defines the divergence of the beam. The neutrons hit the sample and some are scattered. The transmitted (non-scattered) neutrons hit the beam stop on the detector and are used to measure the transmission of the sample. The scattered neutrons are detected on a position-sensitive detector, which is used to measure the cross-section of the sample. The collimation and detector distances are varied to achieve lower or higher resolution.
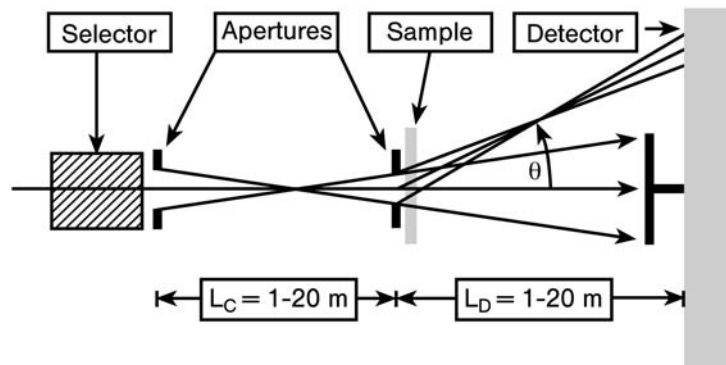

Fig. 1.4 Schematic picture of a SANS experiment.

One assumes that the size of the sample is much smaller than the distances from the source to the sample and from the sample to the detector. The wave fields of the incident and scattered beams are described by the wavevectors $\boldsymbol{k}_i$ and $\boldsymbol{k}_f$ respectively. The scattering vector is defined as the difference between the incident and the scattered wavevectors. The absolute value of the scattering vector for an elastic scattering process is given by

$$Q = |\boldsymbol{k}_i - \boldsymbol{k}_f| = 2k \sin \frac{\theta}{2} = \frac{4\pi}{\lambda} \sin \frac{\theta}{2} \qquad (1.13)$$

where λ is the wavelength of the neutrons adjusted by the velocity selector. The scattering angle θ is depicted in Fig. 1.4.

The elastic scattering function $S(Q,0)$ and the static scattering function $S(Q)$ have been defined above. SANS does not analyze the energy of the scattered neutrons and therefore cannot distinguish between elastic and inelastic scattering processes, i.e. it measures the integral over all energies $S(Q)$. Why can we then use Eq. (1.13), which assumes elastic scattering $k_i = k_f$? SANS accesses large objects or large volumes in real space. As an example, the fast atomic vibrations of a single atom in a polymer chain are not detected by SANS, while the slow motion of the entire macromolecule is. The energy transfer that is detectable in this Q-value regime is in the range $\Delta E < \mu eV$, while the neutrons have energies in the meV range. Therefore, it is justified to assume the scattering to be elastic, although the measured function is $S(Q)$ and not $S(Q,0)$. Equation (1.13) is also applicable for the neutron spin-echo (NSE) technique to be discussed in Section 1.3.1, because $k_i \approx k_f$ still holds. However, as will be explained in detail later, the NSE technique is able to detect the very tiny energy transfers in this Q-value regime by exploiting a property of the neutrons that has not been considered so far.[1]

Since for SANS the detected volumes in the relevant Q-value regime are significantly larger than the volumes of single atoms, the description of the scattering in terms of atomic scattering lengths is not appropriate. As shown below, the coherent scattering is determined by different scattering length densities of volumes which are – with respect to their size – relevant for the Q-values under consideration.

As mentioned above, the Q dependence of the scattering gives information about the structure within the sample. Imagine, for instance, the Bragg equation (first order):

$$\lambda = 2d \sin \frac{\theta}{2} \qquad (1.14)$$

---

[1] Note, however, that even at small angles inelastic scattering processes originating from higher momentum transfers may contribute to $S(Q)$ if the primary forward scattering is not very strong.

Here, d is the distance between lattice planes. Combining Eq. (1.13) with the Bragg equation (1.14) yields $Q = 2\pi/d$, illustrating the relation between the scattering vector and a "typical" distance in the sample.

The resulting scattering intensity should be treated by corresponding reduction procedures to obtain the scattering cross-section, which is independent of the experimental setup and the background. The measured intensity is connected to the cross-section $\mathrm{d}\Sigma/\mathrm{d}\Omega$ by

$$I = I_\mathrm{i} D_\mathrm{e} \Delta\Omega A T d \left(\frac{\mathrm{d}\Sigma}{\mathrm{d}\Omega} \right) \tag{1.15}$$

where I_i is the incident beam intensity, D_e is the detector efficiency, A is the irradiated sample area, d is the sample thickness, T is the sample transmission, and $\Delta\Omega$ is the angle of one detector element. For the absolute calibration, a reference material with a flat cross-section in the measured Q range can be used (e.g. Lupolene).

The structure factor is given by

$$S(Q) = \frac{\mathrm{d}\Sigma/\mathrm{d}\Omega}{K} \tag{1.16}$$

where K is the contrast factor, which describes the interaction of the neutrons with the sample. Let us, for instance, consider a two-component system like a polymer in a solution. Then K is given by $\Delta\rho^2$, where $\Delta\rho$ is the difference in the coherent scattering length densities of the polymer and the solution.

Neutron Spin-Echo (NSE) Spectroscopy

How do these large objects move? As we have seen above, we need to detect the intensity scattered at small angles. However, if we would like to follow the motion of such an object, what is the time scale involved? One can imagine that – in contrast to atomic vibrations, for example – the velocity of these large objects is very low. Imagine a drop of honey that flows from a spoon – it may have a velocity of a few millimeters per second. In contrast to that, neutrons have a velocity of a few hundred meters per second, which in turn means that we would like to detect a velocity change of neutrons in the order of 10^{-5}, at small angles.

In this section we will introduce neutron spin-echo (NSE) spectroscopy, which combines small-angle scattering with the desired energy resolution. To get that high energy resolution, a trick is needed where the neutron spin plays an important role. Instead of using a trick, we could also try to cut from an incoming neutron beam – with a Maxwellian distribution of velocities – a band that is narrow enough to allow for a detection of velocity changes in the order of 10^{-5} by removing all neutrons with unwanted velocity. But then the

remaining intensity would be so poor that a scattering experiment would not be feasible in a realistic time frame.

The essence of the NSE technique is a method to decouple the detectability of tiny velocity changes caused by the scattering process from the width of the incoming velocity distribution. This allows one to run NSE instruments with 10–20% width of the velocity distribution yielding about 10^4 times more neutrons in the primary beam than the direct 10^{-5} filtering. The neutron spin is the key element to realize this decoupling. The basic NSE instrument invented by F. Mezei (Mezei 1980) works as follows (see also Fig. 1.5). A beam of longitudinally polarized neutrons, i.e. neutrons with spins pointing into the beam direction, enters the instrument and traverses a $\pi/2$ flipper located in a low longitudinal magnetic field. During the passage of this flipper, the neutron spins are rotated by $\pi/2$ and are then perpendicular to the beam, e.g. the spins are all pointing upward. Immediately after leaving the flipper, they start to precess around the longitudinal field generated by the primary precession solenoid. As they proceed into the precession coil, the Larmor frequency Ω_L, which is proportional to the field, increases up to several MHz (e.g. about one turn per 0.1 mm length of path) in the middle of the solenoid. The field and Ω_L decrease to low values again on the way to the sample. Upon arriving at the sample, the neutron may have performed many thousand precessions. Keeping in mind that different neutrons with velocities different from the incoming 10–20% distribution have total precession angles that differ proportionally, the ensemble of neutron spins at the sample contains any spin direction perpendicular to the longitudinal field with virtually equal probability.
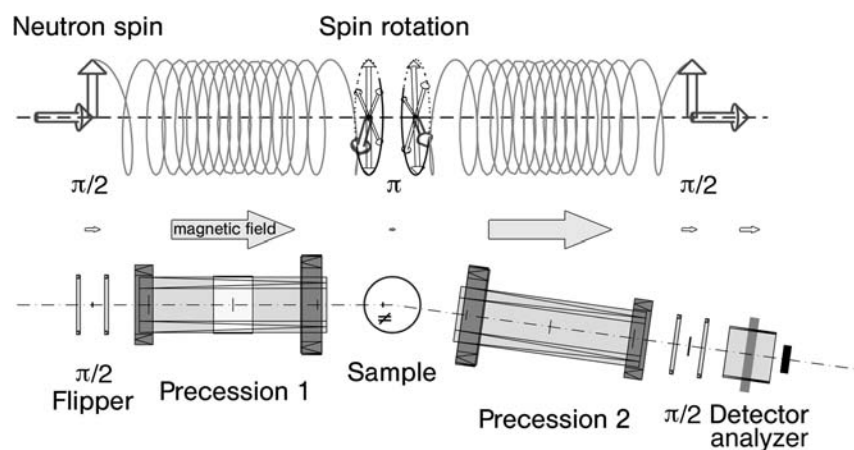
Fig. 1.5 Schematic picture of the geometry of a NSE spectrometer (Monkenbusch et al. 1997).

Nevertheless, each single neutron is tagged with respect to its velocity by the individual precession angle (modulo 2π) of its spin. The spin therefore can be viewed as the neutron's own stopwatch. Now near to the sample position there is a π flipper which, during passage of the neutron, turns its spin by π around an upward-pointing axis. Thereby the sign of the accumulated precession angle is reversed, i.e. the "spin stopwatch" times are set to their negative values. Then the neutrons enter the secondary part of the spectrometer, which is symmetric to the primary part. During the passage of the second main solenoid, provided the sample did not change the neutrons' velocity, each spin undergoes exactly the same number of precessions as in the primary part. Due to the reversing action of the π flipper, this leads to the result that all neutron spins arrive at the same precession angle, pointing upwards, at the second $\pi/2$ flipper, irrespective of their individual velocity. This effect is called the *spin-echo* in analogy to similar phenomena in conventional nuclear resonance experiments. The $\pi/2$ flipper turns these spins by $90°$ into the longitudinal direction. This switches off any effect of the precession on the longitudinal spin polarization. Further down the neutrons enter an analyzer that transmits only neutrons with axially parallel (or antiparallel) spins to the detector. If now the neutrons undergo a velocity change Δv_s in the course of scattering by the sample, the final spin direction is rotated by an amount proportional to Δv_s with respect to the upward direction of the echo. The second $\pi/2$ flipper rotates the upward (echo) direction into the longitudinal direction. Thereby the precession angle with the echo direction is preserved (as the angle of the precession cone after the $\pi/2$ flipper) and the time measurement of the "spin stopwatch" is effectively stopped. The subsequent analyzer has a transmission that depends on the longitudinal component of the spin.

Since only the cosine of the pointer angle counts, the analyzer works as a cosine modulating filter. The filter period Δv_c is controlled by the average number of precessions, e.g. by the average neutron velocity and the magnetic field inside the main precession solenoids. Due to the cosine modulating filter function, the NSE instrument measures the cosine transform of $S(Q, \omega)$, the so-called intermediate scattering function $S(Q, t)$:

$$S(Q, t) \propto \frac{1}{2} \left[S(Q, 0) \pm \int \cos \left(\underbrace{J \lambda^3 \gamma \frac{m_\mathrm{n}^2}{2\pi h^2}}_{t} \omega \right) S(Q, \omega) \, \mathrm{d}\omega \right] \qquad (1.17)$$

where $J = \int_\mathrm{path} |\boldsymbol{B}| \, \mathrm{d}l$ is the integral of the magnetic induction along the flight path of the neutron from the $\pi/2$ flipper to the sample, and $\gamma = 1.830\,33 \times 10^8$ radian s^{-1} T^{-1} is the gyromagnetic ratio. The sign of the integral depends on the type of analyzer and on the choice of the sign of the flipping angle of the secondary $\pi/2$ flipper. The time parameter,

$t = J\lambda^3\gamma m_{\mathrm{n}}^2/(2\pi h^2)$, may be easily scanned by varying the main solenoid current I_0 to which J is (approximately) proportional.

Note that the maximum achievable time t, e.g. the resolution, depends linearly on the (maximum) field integral and on the cube of the neutron wavelength λ!

The fact that the instrument measures the intermediate scattering function directly makes it especially useful for relaxation-type scattering because the relaxation function is measured directly as a function of time. Furthermore, the correction for instrumental resolution is easier. For instruments that measure $S(Q,\omega)$, the correction for the instrumental resolution function $R'(Q,\omega)$ has to be realized by a tedious deconvolution. For NSE, a simple point-by-point division by the result of a measurement of an elastically scattering reference sample is sufficient (Mezei 1980; Monkenbusch et al. 2004). The resolution leads to a decreasing $R(Q,t)$ with increasing Fourier time for purely elastic scattering, where it would be unity for ideal instrument resolution. This is mainly caused by the fact that the neutrons travel slightly different paths leading to different field integrals and therefore to a dephasing of the echo signal. This decay is accounted for by dividing the sample signal $S(Q,t)$ by $R(Q,t)$.

What is the meaning of the scattering function measured by NSE? This depends on the sample. For a deuterated polymer matrix that contains some (about 10–15%) protonated chains, $S(Q,t)$ is dominated by the *coherent* single-chain dynamic structure factor in the SANS regime. The scattering is determined by the difference in scattering length density between the protonated test chains and the environment (the deuterated matrix) as explained in the section about the SANS technique. For low Q-values the coherent scattering is dominant (see Fig. 1.6). The higher the Q-values, the more important becomes the incoherent background from the protonated chains as well as from the smaller incoherent scattering of deuterium. At the intersection of the dashed and thick solid lines in Fig. 1.6, the two contributions have equal magnitude and, since the incoherent signal is phase-shifted by π (see below), the echo signal may even vanish in a certain region of Q and t.

For a sample that contains only fully protonated chains, the *incoherent* scattering function is measured, which reflects the self-correlation of the protons – or in the Q-value range discussed here – of the chain segments. We may call this the segmental self-correlation function. It can be derived easily from Eq. (1.12) in Section 1.3.1 for a Gaussian chain. The derivation and the definition of a Gaussian chain will be discussed in detail below. The result for the incoherent scattering function may be anticipated at this point:

$$S_{\mathrm{inc}}(Q,t) = \exp[-\tfrac{1}{6}Q^2\langle r^2(t)\rangle] \tag{1.18}$$

From this scattering function, the segmental mean square displacement $\langle r^2(t)\rangle$ can easily be extracted.
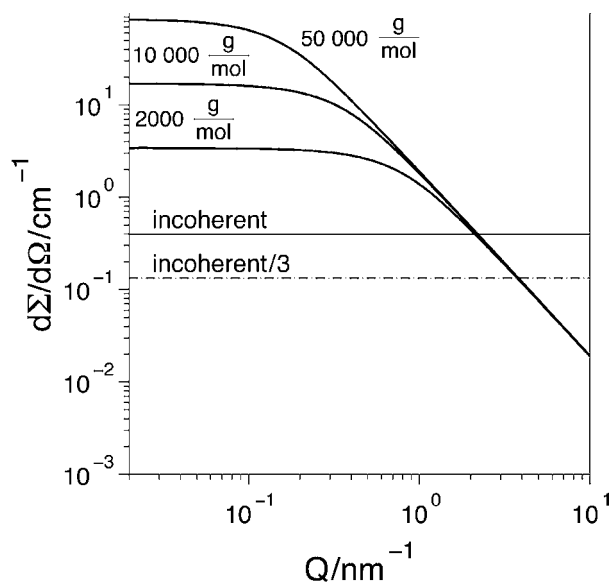
Fig. 1.6 Distribution of coherent and incoherent scattering intensity computed for polyethylene (PE) melts of $M_w = 50\,000$, 10000 and 2000 g mol^{-1} containing 15% (volume fraction) of H-labeled chains and the levels of incoherent background. At the intersection of the polymer structure factors (thick solid lines) with the dashed line, representing one-third of the incoherent scattering (spin flip, see text), the two contributions have equal magnitude. Increasing the amount of labeled component shifts the limit to higher Q-values. For a fully (100%) protonated sample, the incoherent level is higher by a factor of 100/15. On the other hand, to have a reasonable transmission, the sample volume has to be lower by a factor of 10. Therefore, the lines give a realistic estimate for the ratio of the coherently (with 15% protonated chains in a deuterated matrix) and the incoherently scattered intensity.

However, incoherent scattering has some difficulties. Two-thirds of the spin incoherent scattering events flip the neutron spin (Squires 1978); the one-third spin-flipped neutrons compensate the one-third that are not flipped. In the end the resulting intensity consists of one-third spin-flipped neutrons (i.e. the echo is phase-shifted by π compared to a coherent signal) on a background of two-thirds depolarized neutrons:

$$1\uparrow \quad \underbrace{\text{-----}>}_{\text{incoherent scattering}} \quad \tfrac{2}{3}\downarrow + \tfrac{1}{3}\uparrow = \tfrac{1}{3}\downarrow + \text{depolarized background} \qquad (1.19)$$

What is even more important is the fact that the incoherent intensity lacks any amplifying interference effects and, as a sum from N independent point-like centers, it is scattered into the full solid angle, in contrast to the coherent scattering, which focusses most of the intensity in the low-Q region according

to the coherent structure factor. Fig. 1.6 shows calculated scattering intensities for a polymer with three different molecular weights. The shape of the scattering function is discussed in Section 1.4; here we focus on the intensities. As described above, the dashed line in Fig. 1.6 refers to the incoherent scattering of protonated chains (15%) in a deuterated matrix (taking into account the factor 1/3 due to the spin flip). The incoherent scattering of a fully protonated sample will be higher by a factor 100/15. On the other hand, the thickness of typical incoherent samples must be lower by a factor of about 10 to get a reasonable transmission. This leads to the fact that the dashed line in Fig. 1.6 gives a good estimate for the incoherent scattering intensity of a fully protonated sample. Comparing the two intensities, we realize a difference of up to two orders in magnitude (depending on the molecular weight of the labeled chains). Due to the low incoherent intensity, the sample and the background have to be measured carefully and for long times. This requires an extremely stable instrument configuration.

1.3.2
Rheology

Now we will make an excursion from molecules to the macroscopic properties of polymers. The term "rheology" is derived from the Greek word *rheos* (flow); it measures and describes the relation between elongation or shear displacement and stress or torque for different materials.

Looking at a polymer at low temperature, we mainly observe elastic properties. Heating up the material, however, reveals liquid-like characteristics. Instead of varying the temperature, we may focus on different time scales. A very short, shock-like impact on a water surface illustrates that a liquid can be very stiff at short time scales. Elasticity and viscosity – viscoelasticity – are the keywords related to macroscopic properties of polymer systems which can be explored by observing the response of the material to mechanical forces over a broad frequency range. The elasticity leads to deformation, while the viscosity causes the flow of the material. Elastic deformation is a change to the molecular configuration associated with the storage of energy (like in a spring) while flow is an irreversible dissipative process.

A typical mechanical perturbation that can be applied to the system is a small-amplitude oscillatory shearing. This is realized in a rheometer with, for example, parallel disks, where one of the disks rotates with frequency ω. The oscillatory deformation (strain) is then

$$\gamma(t) = \gamma_0 \sin(\omega t) \qquad (1.20)$$

By definition and using the Boltzmann linear superposition of the strain history for a viscoelastic body (Ferry 1970), the resulting time-dependent stress

is given by

$$\sigma(t) = \gamma_0[G'(\omega)\sin(\omega t) + G''(\omega)\cos(\omega t)] =: \gamma_0 G(t). \qquad (1.21)$$

The frequency-dependent moduli are obtained by a Fourier transformation of the relaxation function $G(t)$:

$$G'(\omega) = \omega \int_0^\infty G(t)\sin(\omega t)\,\mathrm{d}t \qquad (1.22)$$

$$G''(\omega) = \omega \int_0^\infty G(t)\cos(\omega t)\,\mathrm{d}t \qquad (1.23)$$

Here, $G'(\omega)$ is a measure for the elastic energy stored in the sample, and is therefore called the *storage modulus*. It is in phase with the strain. $G''(\omega)$ is a measure for the energy that is dissipated in the system (viscous dissipation), and is called the *loss modulus*. It is out of phase with the strain by $\pi/2$. We will focus here on small-amplitude deformations, i.e. on the linear viscoelastic regime.

Let us investigate the response in the two extreme cases of a Newtonian fluid and an elastic solid. For the Newtonian fluid, the shear stress is proportional to the shear rate, with the viscosity η as the constant of proportionality. This means that the modulus G', which reflects the elastic response, vanishes, while $G'' = \eta\omega$ is a linear function of the frequency.

For the second extreme case of an ideal elastic solid, the shear stress is proportional to the strain (Hooke's law for small deformations), with a constant of proportionality G_0. Here, $G'' = 0$ and $G' = G_0$. For a viscoelastic material, we expect a viscous behavior at low frequencies (long times) and an elastic behavior at high frequencies (short times), which should be reflected in a constant G' and for low frequencies in a linear increase of G'' with frequency.

To explore the short-(long-)time behavior, first the frequency window of the rheometer is exploited. If the maximum frequency ω_{max} of the rheometer is reached, one could fix the frequency at ω_{max} and lower the temperature. Then $1/\omega_{\mathrm{max}}$ fixes the time scale and, by decreasing the temperature, faster processes are shifted into this particular time window, i.e. they become "visible". Qualitatively it is obvious that the response now refers to a virtual higher frequency, because the system becomes stiffer with decreasing temperature. The same holds for increasing the temperature at fixed ω_{min}, which relates to "virtually" lower frequencies. Then $1/\omega_{\mathrm{min}}$ determines the longest time scale, and increasing the temperature speeds up slow processes, which thereby shift into the accessible time window. If the relation between time (or frequency) and temperature is known for all relaxation processes in the sample, the vari-

ation of temperature allows the accessible frequency range to be expanded to typically eight to ten decades instead of three.

This time–temperature superposition is valid for most polymers above their glass transition temperature. Rheologically simple behavior means that a single horizontal shift factor a_T for all relaxations in these viscoelastic systems yields a master curve, if, additionally, a vertical shift factor b_T, which relates the strength of the relaxations to temperature, is applied (Ferry 1970; Gotro and Graessley 1984). Usually the Williams–Landel–Ferry (WLF) law for a_T applies (Ferry 1970):

$$\log(a_T) = \left[\frac{-c_1(T - T_0)}{c_2 + (T - T_0)} \right] \tag{1.24}$$

At $T = T_0$, where T_0 is the reference temperature, a_T as well as b_T are unity; c_1 and c_2 are material-specific constants that themselves also depend on T_0. Fig. 1.7 shows how the typical frequency range of an instrument is extended by performing a time–temperature sweep and applying time–temperature superposition.

The lower part of Fig. 1.7 shows the time–temperature superposition for a polyisoprene sample. The storage modulus shows a pronounced plateau at intermediate frequencies. This plateau is a signature of elasticity before the polymer melt starts to flow at lower frequencies (or longer times). It has been demonstrated that the plateau region expands to lower frequencies when the molecular weight is increased while the high-frequency behavior remains constant (Onogi et al. 1970). The plateau, i.e. the elastic behavior at intermediate times, which becomes more dominant the longer the chains are, is one of the most important features in long-chain polymer melts. It will play a fundamental role in this chapter.

1.4
Static Properties

To describe the basic static properties of a polymer chain, let us take polyethylene as an example. There the CH_2 units are linked together as shown in Fig. 1.8. The bond length l_0 between the carbon atoms is fixed. We now consider the model of a freely jointed chain as shown schematically in Fig. 1.9. It assumes N consecutive backbone bonds that have no restrictions on the bond angles, the only condition being that l_0 is fixed. One may then ask for the end-to-end distance vector:

$$\boldsymbol{R}_{\text{ee}} = \sum_{i=1}^{N} \boldsymbol{r}_i \tag{1.25}$$
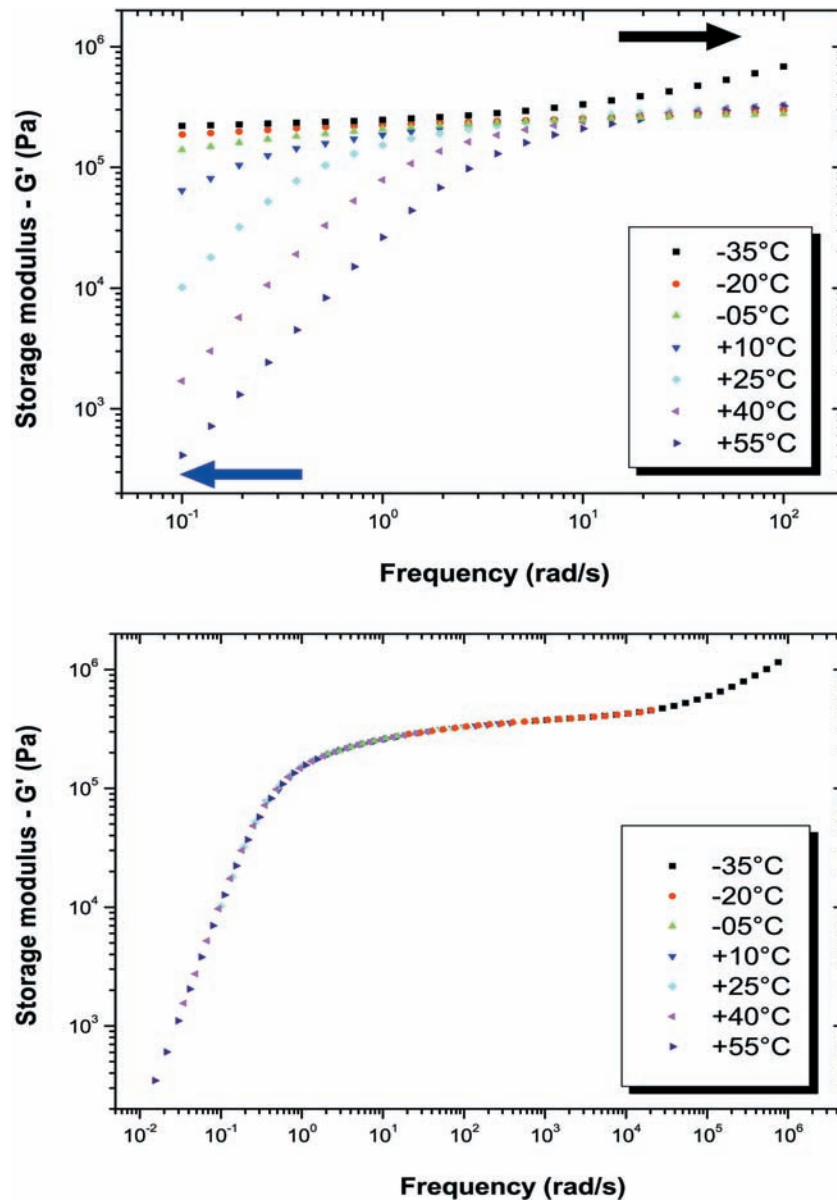
Fig. 1.7 Principle of time–temperature superposition. The frequency range of the instrument is three orders of magnitude (upper figure). By measuring at different temperatures and applying horizontal time–temperature superposition to a reference temperature (here 25 °C) as well as a vertical T-dependent correction, the range is extended to about eight orders of magnitude (lower figure). Data are from a polyisoprene sample with a molecular weight of $M_{\mathrm{w}} = 250$ kg mol^{-1} (Blanchard 2004).
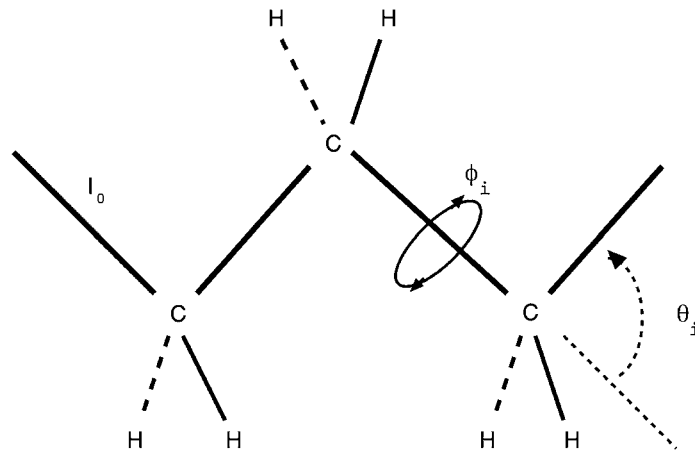
Fig. 1.8 Schematic sketch of a polyethylene chain with definitions of angles: θ_i is the bond angle, and ϕ_i is the torsional angle.
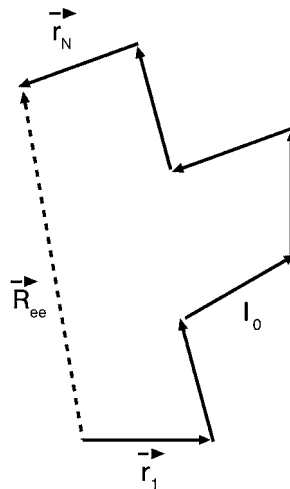
Fig. 1.9 A sketch of a freely jointed chain. The bond vector has a constant length l_0, but the angle is totally free. The end-to-end distance $\boldsymbol{R}_{ee}$ is described by the sum of all bond vectors.

The end-to-end distance vector is defined as the sum of all the bond vectors connecting two consecutive monomers (since $\boldsymbol{r}_{i,j}$ connects the monomers i and j, we define $\boldsymbol{r}_i \equiv \boldsymbol{r}_{i-1,i}$). Since there is no restriction concerning the bond angles – only the bond length is fixed – the chain has no preferential direction. This means that the average of the end-to-end distance – and of every other vector in the system – has to be zero.

The second moment is the average of

$$\boldsymbol{R}_{\text{ee}}^2 = \sum_{i,j=1}^{N} \boldsymbol{r}_i \cdot \boldsymbol{r}_j = \sum_{i=1}^{N} \boldsymbol{r}_i^2 + 2 \sum_{1 \le i < j \le N} \boldsymbol{r}_i \cdot \boldsymbol{r}_j \qquad (1.26)$$

Since in our simple model we have no correlation of different bonds, the averaging leaves a contribution only from the first part of Eq. (1.26):

$$\left\langle \boldsymbol{R}_{\text{ee}}^2 \right\rangle = \sum_{i=1}^{N} \left\langle \boldsymbol{r}_i^2 \right\rangle + 2 \times 0 = N l_0^2 \qquad (1.27)$$

The result of our simple model, that the end-to-end distance is proportional to the square root of N, holds also for more general models. Assuming a chain with fixed bond length *and* fixed angle between the bonds, which can rotate freely around the bonds, again gives the same scaling of the end-to-end distance. In fact, one can show that in general, as long as a chain is subject to any local restriction, in all models for flexible polymer chains the characteristic size increases with the square root of N.

This dependence on the number of segments shows that the characteristic size of a chain is much smaller than the full extension (a stretched chain). Only for a rigid rod-like chain is the end-to-end distance just the number of segments times their length, i.e. it is proportional to N.

At this point it might be helpful to remember the basic law for the diffusion of a particle, which is given by a continuous random walk. To travel a distance R, the particle must make

$$N = \left(\frac{R}{l_0} \right)^2 \qquad (1.28)$$

steps, where l_0 is the mean free path. That means that the chain conformation is nothing other than a random walk with a "step length" given by the bond length l_0 and the number of steps given by the number of bonds N. The end-to-end distance then represents the distance the particle has traveled.

Next to the end-to-end distance, the radius of gyration is often used to describe the chain size. It measures the size of a molecule in the manner of a moment of inertia. The vectors of all monomers relative to the center of mass are squared (assuming the same weight of all monomers). This sum is normalized by the number of monomers. The radius of gyration therefore measures the average extension of a chain relative to the center of mass. Without derivation we write

$$\left\langle \boldsymbol{R}_{\text{g}}^2 \right\rangle = \tfrac{1}{6} \left\langle \boldsymbol{R}_{\text{ee}}^2 \right\rangle \qquad (1.29)$$

It is obvious that real chains are not random walks where the angle between two steps is randomly distributed in a mathematical sense. The probability for high angles is lower compared to low angles due to the stiffness of the chains. The stiffness of a chain will depend on its chemical structure, side groups, etc. Therefore we will introduce a stiffness parameter C_∞ with

$$l^2 = C_\infty l_0^2 \tag{1.30}$$

and call l the effective bond length.

Before discussing the Gaussian chain, we define the frequently used Kuhn segment length. A model-independent parameter for polymer chains is the contour length L, which is calculated by multiplying the number of effective bonds by their length, $L = Nl$. Now, it is obvious that one can divide the chain into (arbitrary) larger segments l' in such a way that the contour length $L = N'l'$ is constant. One important definition of such an l' is the Kuhn segment length l_K, which is a measure for the distance over which correlations between bond vectors are lost. The idea is quite simple. If the number of bonds per segment l_K is large enough to erase any correlation between different Kuhn segments, the chain can be regarded as a freely jointed chain with N_K segments of length l_K. This means that real polymer chains, as long as they are long enough, can be mapped to a freely jointed chain. The Kuhn segment length is defined by

$$l_K = C_\infty l_0 \tag{1.31}$$

The Gaussian chain is a more general model of a freely jointed chain. The idea is that the number of bonds in a segment of a Gaussian chain is already sufficiently large that the distribution function of a single segment can be approximated by a Gaussian distribution. Then the distribution function of such N_K segments can be written as

$$W(\boldsymbol{r}_1, \ldots, \boldsymbol{r}_{N_K}) = \left(\tfrac{2}{3}\pi l_K^2\right)^{-3N_K/2} \exp\left(-\frac{3}{2l_K^2}\sum_i \boldsymbol{r}_i^2\right) \tag{1.32}$$

or, using the difference of monomer vectors instead of the effective bond vectors,

$$W(\boldsymbol{R}_0, \ldots, \boldsymbol{R}_{N_K}) = \left(\tfrac{2}{3}\pi l_K^2\right)^{-3N_K/2} \exp\left(-\frac{3}{2l_K^2}\sum_i (\boldsymbol{R}_i - \boldsymbol{R}_{i-1})^2\right) \tag{1.33}$$

This distribution function can be compared with a thermodynamic partition function:
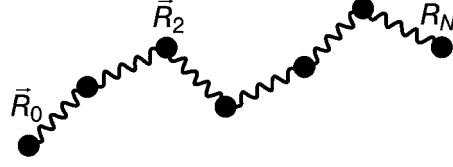
Fig. 1.10 A Gaussian chain represented by a number of effective monomers, which are connected by elastic springs (the spring–bead model).

$$W \propto \exp\left(-\frac{1}{k_{\mathrm{B}}T}\underbrace{\frac{3k_{\mathrm{B}}T}{2l_{\mathrm{K}}^2}\sum_i(\boldsymbol{R}_i - \boldsymbol{R}_{i-1})^2}_{\text{Hamiltonian}}\right) \tag{1.34}$$

where T is the temperature and k_{B} the Boltzmann constant. The Hamiltonian in Eq. (1.34) describes N_{K} Hookean entropic springs with a single temperature-dependent spring constant. The Gaussian chain can therefore be described as beads connected by N_{K} hypothetical springs, the spring–bead model (see Fig. 1.10).

Let us now discuss how the size of a polymer chain can be measured. As discussed in Section 1.3 the structure factor $S(Q)$ can be measured by SANS. We will see in the following that the size of a polymer in terms of, for example, the radius of gyration R_{g} can be directly extracted from the measured $S(Q)$. The static structure factor for a single chain is given by a sum over all possible pairs of monomers i, j reflecting all possible interferences of elementary waves originating from monomer pairs. We calculate $S(Q)$ for a Gaussian distribution of the $\boldsymbol{R}_i - \boldsymbol{R}_j$ (Gaussian chain):

$$S(Q) = \frac{1}{N}\sum_{i,j}^{N}\left\langle\exp\left[\mathrm{i}\boldsymbol{Q}(\boldsymbol{R}_i - \boldsymbol{R}_j)\right]\right\rangle \tag{1.35}$$

$$= \frac{1}{N}\sum_{i,j}^{N}\exp\left\langle-\tfrac{1}{2}[\boldsymbol{Q}(\boldsymbol{R}_i - \boldsymbol{R}_j)]^2\right\rangle \tag{1.36}$$

$$= \frac{1}{N}\sum_{i,j}^{N}\exp\left\langle-\tfrac{1}{6}\boldsymbol{Q}^2(\boldsymbol{R}_i - \boldsymbol{R}_j)^2\right\rangle \tag{1.37}$$

$$= \frac{1}{N}\sum_{i,j}^{N}\exp[-\tfrac{1}{6}l^2Q^2\,|i-j|\,] \tag{1.38}$$

$$= \frac{1}{N}\int_0^N\mathrm{d}i\int_0^N\mathrm{d}j\,\exp(-\tfrac{1}{6}Q^2\,|i-j|\,l^2) \tag{1.39}$$

We will discuss Eqs. (1.35) to (1.39) step by step. Equation (1.36) is obtained from Eq. (1.35) by Gaussian transformation (only valid for Gaussian chains); the next step is the result of an average projection. The averaging is executed from Eq. (1.37) to Eq. (1.38). Finally, we replace the summation by an integration, which is correct for a Gaussian chain with a large number of monomers N. The result of this double integral reads

$$S(Q) = \frac{2N}{R_{\mathrm{g}}^4 Q^4}[\exp(-R_{\mathrm{g}}^2 Q^2) - 1 + (R_{\mathrm{g}}^2 Q^2)] \qquad (1.40)$$

which is the so-called Debye function. The asymptotic form of $S(Q)$ is given by

$$S(Q) = \begin{cases} N(1 - R_{\mathrm{g}}^2 Q^2/3) & \text{for } QR_{\mathrm{g}} \ll 1 \\ 2N/R_{\mathrm{g}}^2 Q^2 & \text{for } QR_{\mathrm{g}} \gg 1 \end{cases} \qquad (1.41)$$

The Debye function may be approximated by the simpler form:

$$S(Q) = \frac{N}{1 + Q^2 R_{\mathrm{g}}^2/2} \qquad (1.42)$$

Fig. 1.11 shows the Debye function and different approximations.
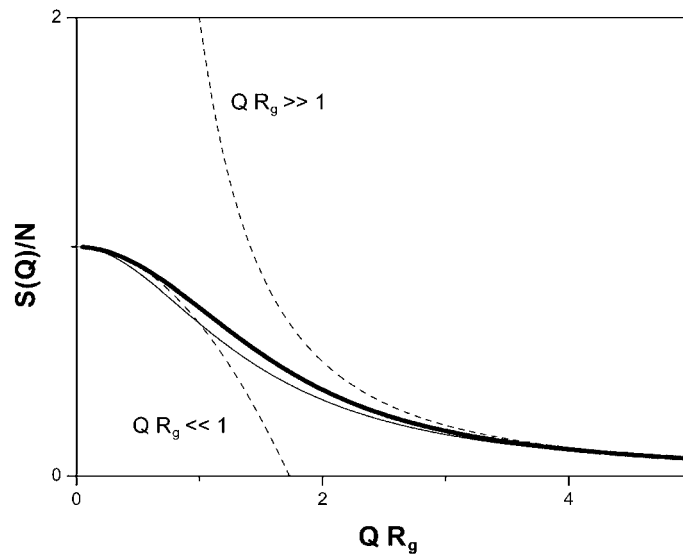
Fig. 1.11 The Debye function normalized by N versus QR_{g} (thick solid line). The dashed lines represent the asymptotic forms, and the thin solid line is the approximation of Eq. (1.42).
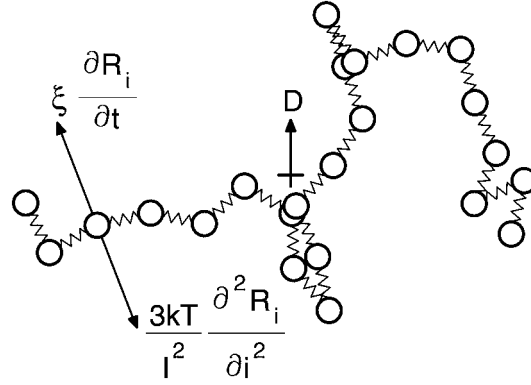
Fig. 1.12 Spring–bead model of a Gaussian chain as assumed in the Rouse model. The two arrows on the left side illustrate the forces as indicated on the left-hand side of Eq. (1.44). D represents the center-of-mass diffusion.

1.5
Brownian Motion, Viscous and Entropic Forces: the Rouse Model

We now consider the dynamics of a Gaussian chain in terms of the so-called Rouse model. We will start with a Gaussian chain, which we now consider as a coarse-grained polymer model where beads represent several monomers connected by hypothetical springs (see Fig. 1.12). It has been shown in Section 1.4 that the spring–bead model is an equivalent description of a Gaussian chain.

The equation of motion contains the entropic springs $k = 3k_{\mathrm{B}}T/l^2$ as the source of restoring forces, a simple local friction ξ as the sole interaction of the chain with the embedding melt of identical chains, and a random force $\boldsymbol{f}_i(t)$ with

$$\langle f_{i\alpha}(t_1)f_{j\beta}(t_2)\rangle = 2k_{\mathrm{B}}T\xi\delta_{ij}\delta_{\alpha\beta}\delta(t_1 - t_2)$$

representing the interaction with the heat bath. Here, α and β denote the Cartesian components. The resulting Langevin equation is

$$\xi\frac{\mathrm{d}\boldsymbol{R}_i}{\mathrm{d}t} - \frac{3k_{\mathrm{B}}T}{l^2}(\boldsymbol{R}_{i+1} - 2\boldsymbol{R}_i + \boldsymbol{R}_{i-1}) = \boldsymbol{f}_i(t) \tag{1.43}$$

Assuming a continuous index variable i we obtain

$$\xi\frac{\partial\boldsymbol{R}_i}{\partial t} - \frac{3k_{\mathrm{B}}T}{l^2}\frac{\partial^2\boldsymbol{R}_i}{\partial i^2} = \boldsymbol{f}_i(t) \tag{1.44}$$

with the boundary conditions $(\partial \boldsymbol{R}_i/\partial i)|_{i=0,N} = 0$. The solution is obtained by a transformation to normal coordinates

$$\boldsymbol{X}_p(t) = \frac{1}{N} \int_0^N \mathrm{d}i \, \cos\left(\frac{p\pi i}{N}\right) \boldsymbol{R}_i(t) \tag{1.45}$$

yielding

$$2N\xi \frac{\partial \boldsymbol{X}_p}{\partial t} + \frac{6k_{\mathrm{B}}T\pi^2}{Nb^2} p^2 \boldsymbol{X}_p = \boldsymbol{f}_p(t) \tag{1.46}$$

Here, $\boldsymbol{f}_p(t)$ are again random forces that are independent of each other. The transformation of Eq. (1.44), which describes coupled oscillators, to Eq. (1.46), is realized by a set of normal coordinates $\boldsymbol{X}_p(t)$, which can move independently, and therefore allows a description of the dynamics of the polymer chain by independent motions, which are called "modes" p.

The correlation functions for $p > 0$ are given by

$$\langle X_{p\alpha}(t) X_{q\beta}(t) \rangle = \delta_{\alpha\beta}\delta_{pq}k_{\mathrm{B}}T \frac{Nl^2}{3k_{\mathrm{B}}T2\pi p^2} \exp\left(-t\frac{p^2}{\tau_{\mathrm{R}}}\right) \tag{1.47}$$

with

$$\tau_{\mathrm{R}} = \frac{\xi N^2 l^2}{3\pi^2 k_{\mathrm{B}}T} \tag{1.48}$$

where τ_{R} is called the Rouse time.

Mode $p = 0$ denotes the center-of-mass diffusion, which is exactly the Einstein expression for the diffusion of a particle with friction coefficient $N\xi$:

$$\langle X_{0\alpha}(t) X_{0\beta}(0) \rangle = \delta_{\alpha\beta} \frac{2k_{\mathrm{B}}T}{N\xi} t \tag{1.49}$$

The scattering of the polymer chain is obtained by the summation of the segmental scattering amplitudes lumped into the beads with the proper phase factors:

$$S(Q,t) = \frac{1}{N} \left\langle \sum_{i,j=1}^N \exp[\mathrm{i}\boldsymbol{Q} \cdot (\boldsymbol{R}_i(t) - \boldsymbol{R}_j(0))] \right\rangle \tag{1.50}$$

This is the scattering function defined in Eq. (1.35) but with time-dependent position vectors. In analogy to the calculation in Section 1.4, we can now, under the assumption of a Gaussian chain, calculate the averages $\langle \ \rangle$:

$$\langle \exp[\mathrm{i}\boldsymbol{Q} \cdot (\boldsymbol{R}_i(t) - \boldsymbol{R}_j(0))] \rangle = \exp\left[-\tfrac{1}{6}Q^2 \underbrace{\langle (\boldsymbol{R}_i(t) - \boldsymbol{R}_j(0))^2 \rangle}_{\Phi_{ij}(t)} \right] \tag{1.51}$$

Repeating the steps demonstrated in Section 1.4 in Eqs. (1.35) to (1.38) yields the scattering function:

$$S(Q,t) = \frac{1}{N} \sum_{i,j} \exp[-\tfrac{1}{6} Q^2 \Phi_{ij}(t)] \tag{1.52}$$

The mean square displacement $\Phi_{ij}(t)$ may be decomposed into three contributions:

$$\Phi_{ij}(t) = \Phi_{\mathrm{D}}(t) + \Phi_{ij}^0 + \Phi_{ij}^1(t) \tag{1.53}$$

where $\Phi_{ij}^0 = |i - j| l^2$ describes the correlation due to the structure of the Gaussian chain. Inserting this expression for $\Phi_{ij}(t)$ in Eq. (1.52) reproduces the static structure factor as derived in Section 1.4 (Eq. 1.38), which finally gives the Debye function (Eq. 1.40.)

The dynamics is taken into account by two contributions. The first, $\Phi_{\mathrm{D}}(t) = 6Dt$, is the center-of-mass diffusion, which is, as for any diffusing object, represented by a common factor:

$$S_{\mathrm{diffusion}}(Q,t) = \exp(-Q^2 Dt) \tag{1.54}$$

The second contribution, $\Phi_{ij}^1(t)$, is obtained by first calculating the inverse transform of the normal coordinates as defined in Eq. (1.45):

$$\boldsymbol{R}_i(t) = \boldsymbol{X}_0 + 2 \sum_{p=1} \boldsymbol{X}_p(t) \cos\left(\frac{p\pi i}{N}\right) \tag{1.55}$$

By inserting Eq. (1.55) in $\Phi_{ij}(t)$ as defined in Eq. (1.51) and omitting the diffusion and structural correlations, we get, after some algebraic transformations,

$$\Phi_{ij}^1 = \frac{4Nl^2}{\pi^2} \sum_{p=1} \frac{1}{p^2} \cos\left(\frac{p\pi j}{N}\right) \cos\left(\frac{p\pi i}{N}\right) \left[1 - \exp\left(-\frac{tp^2}{\tau_{\mathrm{R}}}\right)\right] \tag{1.56}$$

representing the internal dynamics of the chain, which vanishes for $t = 0$: $\Phi_{ij}^1(t{=}0) = 0$. Inserting all contributions of $\Phi_{ij}(t)$ (three addends in Eq. 1.53) into Eq. 1.52, we finally get the Rouse scattering function:

$$S(Q,t) = \frac{1}{N} \sum_{i,j} \exp\Bigg\{ -Q^2 Dt - \tfrac{1}{6} Q^2 |i - j| l^2 \tag{1.57}$$

$$-\frac{2Q^2 N l^2}{3\pi^2} \sum_{p=1} \frac{1}{p^2} \cos\left(\frac{p\pi j}{N}\right) \cos\left(\frac{p\pi i}{N}\right) \left[1 - \exp\left(-\frac{tp^2}{\tau_{\mathrm{R}}}\right)\right] \Bigg\}$$

The Rouse model provides a good description of the dynamics of a Gaussian chain. It is valid for real linear polymer chains on an *intermediate* length scale. The specific (chemical) properties of a polymer enter only in terms of two parameters $Nl^2 = 6R_g^2$ and l^2/ξ, i.e. the dimension of the chain and an effective friction. This of course means that for high Q-values, where neutrons start to detect the chemical structure of single monomers, one expects deviations from pure Rouse behavior. Indeed this has been found in simulation and experiments (Paul et al. 1998; Richter et al. 1999).

The friction parameter ξ/l^2 is often expressed in terms of the so-called *Rouse rate*,

$$Wl^4 = 3k_B T l^2/\xi \qquad (1.58)$$

and the center-of-mass diffusion may be expressed as

$$D = \frac{k_B T (l^2/\xi)}{6R_g^2} = \frac{Wl^4}{18R_g^2}. \qquad (1.59)$$

In modeling the Rouse expression (at intermediate Q), the parameters N and l are somewhat arbitrary as long as the physical values l^2/ξ and R_g are kept constant.

What is the static structure factor $S(Q, t=0) = S(Q)$ in the framework of the Rouse theory? Starting from Eq. (1.57) we get

$$S(Q) = \frac{1}{N} \sum_{i,j} \exp(-\tfrac{1}{6}Q^2 |i - j| l^2) \qquad (1.60)$$

Replacing the summations by integrals, we end up with what was derived in Section 1.4 (see Eq. 1.39), i.e. we get the Debye function.

Before comparing the model to experimental data, let us consider the mean square displacement of a single segment in the framework of the Rouse model for very short times. Neglecting the diffusion for short times, we start from Eq. (1.56) and get, for one segment n,

$$\Phi_n^1 = \frac{4Nl^2}{\pi^2} \sum_{p=1} \frac{1}{p^2} \cos^2 \left(\frac{p\pi n}{N} \right) \left[1 - \exp \left(-\frac{tp^2}{\tau_R} \right) \right] \qquad (1.61)$$

Since we are interested in short times, the large p-numbers dominate, and we can replace the $\cos^2$ by the average $1/2$. Transforming the sum into an integral finally yields:[2]

---

[2] Note that the approximate prefactor of Eq. (6.104) in Doi and Edwards (1986) differs from the exact result given here by a factor $\sqrt{12/\pi}$.

$$\Phi_n^1 = \frac{4Nl^2}{\pi^2} \int_0^\infty \mathrm{d}p \, \frac{1}{p^2} \frac{1}{2} \left[1 - \exp\left(-\frac{tp^2}{\tau_{\mathrm{R}}} \right) \right] \tag{1.62}$$

$$= \left(\frac{12 k_{\mathrm{B}} T l^2 t}{\xi \pi} \right)^{1/2} = \left(\frac{4 W l^4 t}{\pi} \right)^{1/2} \tag{1.63}$$

The main result of this approximation is that the mean square displacement of a segment at short times is $\propto t^{1/2}$ in the Rouse model. This represents a sub-Fickian motion due to correlations of displacements along the chain away from the probe monomer n. With Eqs. (1.18) and (1.63) the incoherent scattering function for Rouse dynamics is given by

$$S_{\mathrm{inc}}(Q, t) = \exp\left[-\frac{Q^2}{3} \left(\frac{W l^4 t}{\pi} \right)^{1/2} \right] \tag{1.64}$$

1.5.1
Experimental Studies of the Rouse Model

We have seen in Section 1.3 that the mean square segment displacement can be extracted directly from the incoherent scattering function $S(Q, t)$ by $-6 \ln[S_{\mathrm{inc}}(Q, t)]/Q^2 = \langle r^2(t) \rangle$ (Eq. 1.18).

Incoherent NSE experiments have been performed at the NSE spectrometer at the DIDO research reactor FRJ2 in Jülich, Germany (Monkenbusch et al. 1997) on a fully protonated poly(ethylene–propylene) (PEP) sample of 0.3–0.4 mm thickness and a molecular weight of $M_{\mathrm{w}} = 80 \ \mathrm{kg \ mol^{-1}}$. The wavelength of the incoming neutrons was $\lambda = 0.8$ nm. The data will be discussed in more detail in the next section. Here, we focus on the mean square displacement at short Fourier times. Fig. 1.13 shows the data. Using $W l^4 (T{=}492 \ \mathrm{K}) = 3.26 \ \mathrm{nm^4 \ ns^{-1}}$ (Richter et al. 1993), they are in excellent agreement with the Rouse prediction of Eq. (1.63). Note that the line in Fig. 1.13 was calculated without any adjustable parameter.

Now we will consider the single-chain dynamic structure factor, measured by coherent NSE. In the high-Q regime, where $S(Q) = 2N/(R_{\mathrm{g}}^2 Q^2)$ (see Eq. 1.41), and neglecting the diffusion, the following form for $S(Q, t)$ can be derived (Doi and Edwards 1986):

$$S(Q, t) = \frac{12}{Q^2 l^2} \int_0^\infty \mathrm{d}u \, \exp\left[-u - \sqrt{\Gamma(Q)t} \, h\big(u/\sqrt{\Gamma(Q)t}\big) \right] \tag{1.65}$$

which contains the characteristic relaxation rate

$$\Gamma(Q) = \frac{k_{\mathrm{B}} T}{12 \xi} Q^4 l^2 = \frac{W l^4 Q^4}{36} \tag{1.66}$$
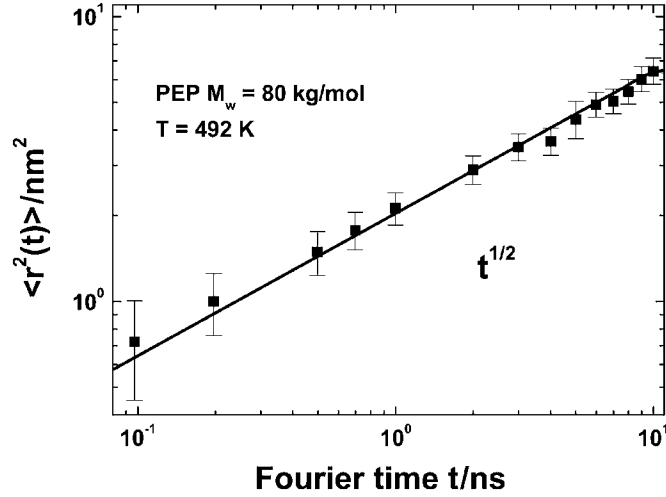
Fig. 1.13 NSE data of protonated PEP (H-PEP) with $M_{\mathrm{w}} = 80$ kg mol^{-1} at 492 K. The scattering vector is $Q = 1$ nm^{-1}. The solid line shows the Rouse prediction.

and

$$h(u) = \frac{2}{\pi} \int_0^\infty \mathrm{d}x \, \cos(xu) \frac{(1 - \mathrm{e}^{-x^2})}{x^2}$$

$$= \frac{2}{\sqrt{\pi}} \, \mathrm{e}^{-u^2/4} + u[\mathrm{erf}(u/2) - 1] \tag{1.67}$$

For $t = 0$, Eq. (1.65) is not the Debye function but yields its high-Q limiting behavior $\propto Q^{-2}$. It is only valid for $QR_{\mathrm{g}} \gg 1$. In that regime the form of $\Gamma(Q)$ immediately reveals that the local (intra-chain) relaxation increases $\propto Q^4$ in contrast to normal diffusion $\propto Q^2$. The form of $S(Q,t)/S(Q)$ obtained from Eq. (1.65) depends on $x = \sqrt{\Gamma(Q)t}$ only. NSE data obtained for different Q plotted versus x should collapse onto a common master curve if the Rouse model is valid, and they indeed do. Fig. 1.14 shows the single-chain dynamic structure factor of 10% H-PEE in a deuterated matrix (D-PEE) in the Rouse scaling representation $[S(Q,t)/S(Q)$ versus the so-called Rouse variable $Q^2 l^2 (Wt)^{1/2}]$ for several Q-values at $T = 473$ K. All data merge onto one master curve. Fig. 1.15 shows $\Gamma(Q)$ as derived from a Rouse fit in the short-time regime of the same data compared to Eq. (1.66) (dashed line). Taking into account center-of-mass diffusion (solid line), excellent agreement is found (Montes et al. 1999).

Fig. 1.16 shows NSE data of PE with $M_{\mathrm{w}} = 2$ kg mol^{-1}, taken at the MESS NSE spectrometer at the LLB, Saclay, France, in the representation
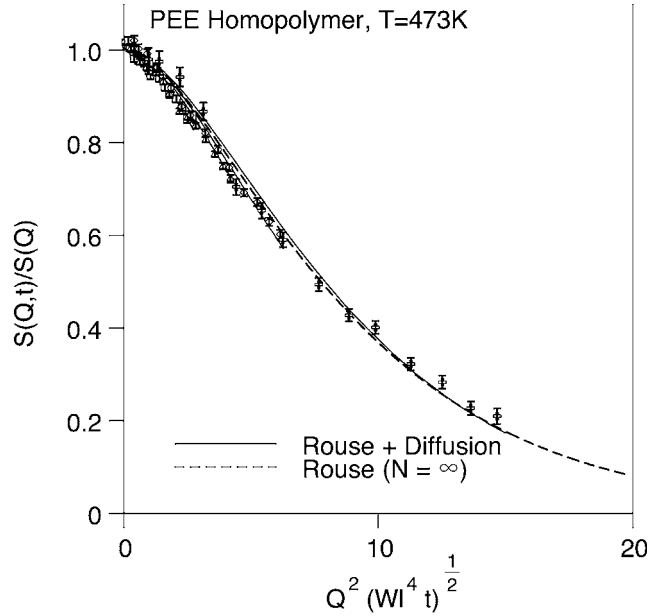
Fig. 1.14 Single-chain dynamic structure factor measured on a melt of 10% protonated polyethylethylene (H-PEE, $M_\mathrm{w} = 21.5$ kg mol^{-1}) in a deuterated matrix of polyethylethylene (D-PEE) ($M_\mathrm{w} = 24.5$ kg mol^{-1}) in a Rouse scaling plot (Monkenbusch et al. 1997; Montes et al. 1999). Shown are seven different Q-values between $Q = 0.5$ and 2 nm^{-1}.

$S(Q,t)/S(Q)$ versus Fourier time t. The data were taken at $T = 509$ K for five different Q-values with a neutron wavelength of $\lambda = 0.6$ nm. The solid lines represent a fit with the Rouse model (Eq. 1.57). Since the segment length $l = l_0\sqrt{C_\infty} = 4.12$ Å (Boothroyd et al. 1991) for polyethylene is known and the number of segments can easily be calculated by $N = M_\mathrm{w}/M_0 = 137$, the only free parameter to fit all Q-values simultaneously is the Rouse rate Wl^4 or the friction coefficient ξ. Fig. 1.16 shows that the data are described perfectly. In conjunction with the agreement demonstrated in Fig. 1.13 for the incoherent data, the dynamic structure factor results demonstrate the validity of the rather simple concept of a chain in a heat bath where the relaxation of thermally activated fluctuations is determined by a balance of viscous forces (velocity, friction) and entropic forces.

For Q-values larger than Q_max (interestingly $Q_\mathrm{max} \approx 1.5\,\mathrm{nm}^{-1}$ seems to be a more or less universal value for many polymers), deviations from the Rouse model are observed. At high Q, effects of local chain stiffness and internal viscosity start to play a role (Richter et al. 1999). However, in the Q-value range shown in Fig. 1.16, the local structure of the polymer chain does not play any role and the Rouse model is valid.
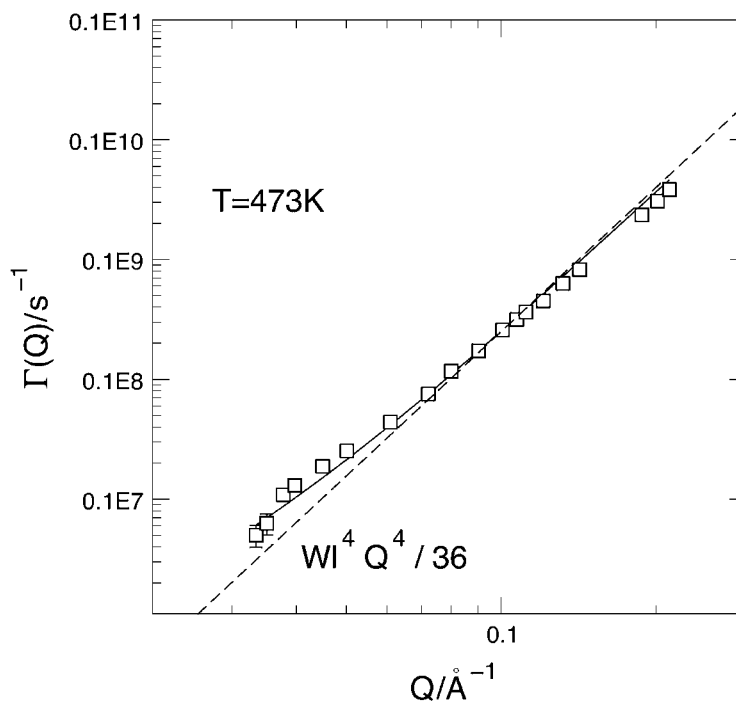
Fig. 1.15 Initial slope extracted from the same PEE data as shown in Fig. 1.14 as a function of Q. The dashed line represents $\Gamma(Q)$ as calculated by Eq. (1.66). The solid line takes translational diffusion into account (Montes et al. 1999).

Fig. 1.17 shows data of PE with $M_{\mathrm{w}} = 12$ kg mol^{-1} measured at the IN15 NSE spectrometer at the ILL, Grenoble, France, in the representation $S(Q,t)/S(Q)$ versus Fourier time t. Due to the availability of a sufficiently high intensity of long-wavelength neutrons [in the case of the data shown in Fig. 1.17, the wavelength is $\lambda = 1.5$ nm (open symbols)], the IN15 holds the world record with respect to resolution (Schleger et al. 1999). Following Eq. (1.17) the maximum Fourier time is proportional to the wavelength cubed. The accessible Fourier time for $\lambda = 1.5$ nm is about 165 ns. However, if the sample is a strong scatterer, one can use neutrons with even longer wavelength (at the cost of intensity), e.g. $\lambda = 2$ nm, which would yield a maximum Fourier time of 390 ns.

The data in Fig. 1.17 were fitted with the Rouse model. Forcing an agreement at very short Fourier times by restricting the fits to 5 or 10 ns, it is evident that the data strongly deviate from the Rouse prediction at longer times. However, the only difference between the samples shown in Figs. 1.16 and 1.17 is the molecular weight, the chains in the latter sample being six times longer
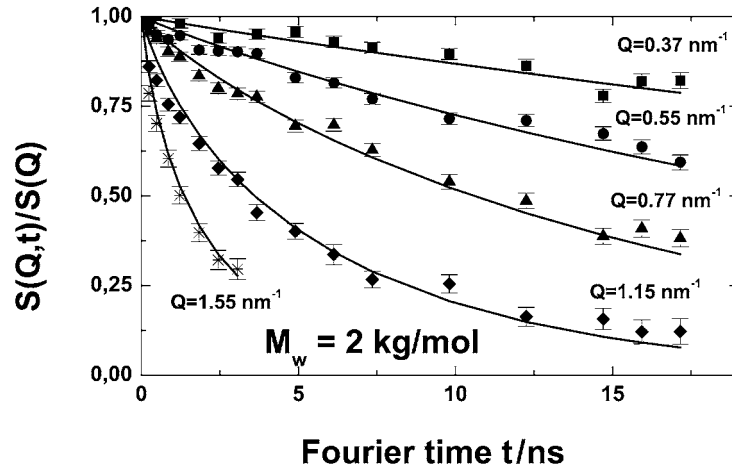
Fig. 1.16 NSE data of PE with $M_\mathrm{w} = 2$ kg mol^{-1} at $T = 509$ K for various Q-values (Richter et al. 1994). The solid lines represent a fit with the Rouse model.
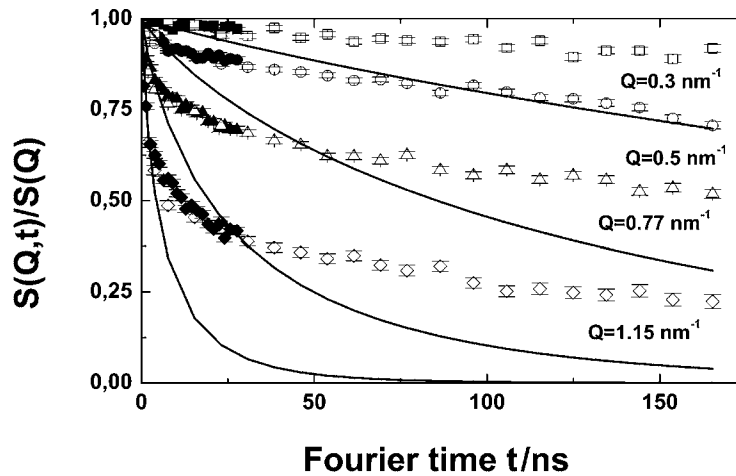

Fig. 1.17 NSE data of PE with $M_\mathrm{w} = 12$ kg mol^{-1} at 509 K for various Q-values. Filled symbols: wavelength of the incoming neutrons $\lambda = 0.82$ nm (maximum Fourier time 28 ns); open symbols: $\lambda = 1.5$ nm (maximum Fourier time 165 ns). The solid lines represent a fit with the Rouse model.

than in the former. For the longer chains the free three-dimensional Rouse-like relaxation is obviously perturbed. After an initial decay of $S(Q, t)$, the relaxation slows down, and we will see later that for even longer chains the relaxation in the NSE time window stops completely.

1.0

0.8

$S(Q,t) / S(Q)$

0.6

0.4

0.2

0

M_w=36 kg/mol

20   40   60   80

$$Q^2 (W l^4 t)^{\frac{1}{2}}$$
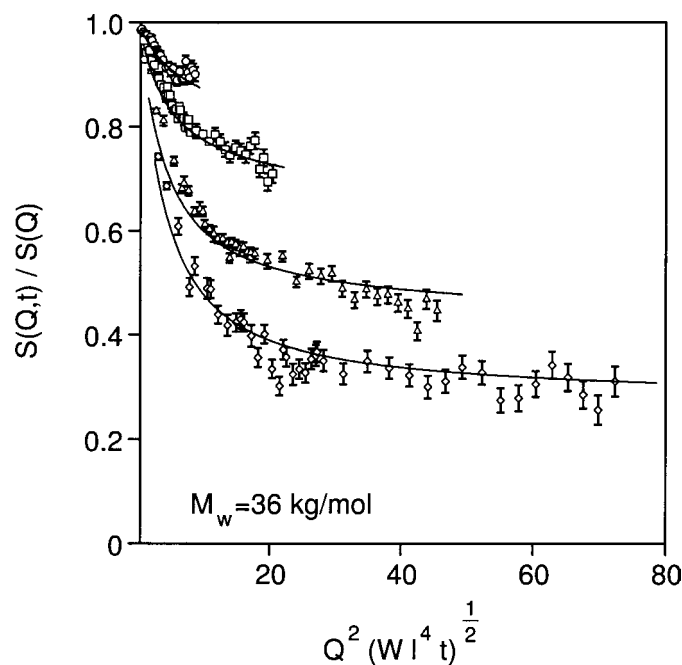
Fig. 1.18 NSE data of PE with $M_w = 36$ kg mol^{-1} at 509 K for various Q-values in a Rouse scaling plot. Lines are guides to the eye.

Fig. 1.18 shows how NSE data from long PE chains look if plotted in the Rouse scaling. In contrast to the data presented in Fig. 1.14 for PEE, here the four shown Q-values of a sample with molecular weight $M_w = 36$ kg mol^{-1} do not at all merge onto one master curve. They show a distinct splitting for different Q-values already at short Fourier times, pointing to a significant deviation from the Rouse picture.

The observation in NSE experiments as illustrated in Figs. 1.17 and 1.18 is in agreement with what has been observed in the storage modulus of long-chain polymer melts. As already briefly discussed in Section 1.3.2, in the range of intermediate frequencies $G'(\omega)$ shows a plateau, which is an indication for elastic behavior. Indeed we will see that the slowing down of relaxation in NSE experiments, on the one hand, and the existence of a plateau in the storage modulus, on the other, have the same origin. They are both indications of what is dominating the dynamics of long-chain polymer systems: topological constraints in terms of entanglements. These prevent the chain from relaxing completely via the Rouse modes by building a kind of temporary network which leads to the observed network-like response in rheology.

In the next section the most successful model to describe these topological constraints is discussed: the tube concept.

1.6
Topological Constraints: the Tube Concept

As we have seen above, in the melt, long-chain polymers interpenetrate each other and restrict their motions. This restriction originates from topological constraints that arise due to the formation of entanglements by the long chains.

In his famous reptation model, P.-G. de Gennes described the effect of these entanglements by a virtual tube along the coarse-grained chain profile, localizing the chain and confining the chain motion (de Gennes 1981; Doi and Edwards 1986) (see Fig. 1.19). The tube follows a random walk and represents the topological confinements. The tube in this concept is not meant as a "chemical" tube, which would have a diameter in the range of the chain–chain distance, i.e. a few tenths of a nanometer. We will see that the diameter d of the virtual tube is much larger.
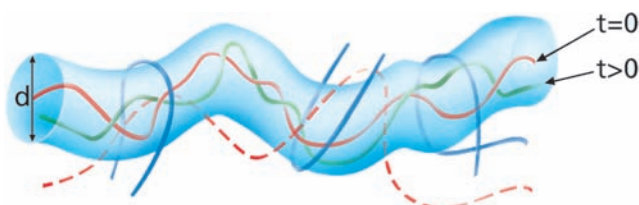
Fig. 1.19 Schematic illustration of the tube concept. The lateral confinement of a polymer chain is represented by a tube with diameter d formed by adjacent chains.

Let us now take a "test chain" confined in such a virtual tube. What kind of motion can this chain execute? First of all, we would expect that our chain does not know that it is confined at very short times. If the mean square displacement of the segments is smaller than half the tube diameter d, no contact of the segments with the virtual walls of the tube will have happened. Therefore, normal Rouse dynamics should be expected in the short-time regime. After this contact has taken place, after a time that we call the "entanglement time" τ_e, the Rouse dynamics can only take place in one dimension along the tube profile, a kind of curvilinear version of the Rouse motion that is called "local reptation" in de Gennes' model.

What happens with the center-of-mass diffusion of the entire chain? Of course, provided the tube exists, diffusion also can take place only along the tube, in one dimension. Since the tube itself is defined as a kind of envelope of the chain, the diffusing molecule follows, and has to follow, its own contour. It is a snake-like motion, which is in the end the reason for calling this the "reptation" model. We will see that this third process is very slow – too slow

to be observed in NSE, even if we use the IN15, which provides the highest resolution in time available in the world.

The introduction of the tube concept for long-chain polymer systems is inevitably connected with the introduction of a new parameter besides the segment length: a second length scale that describes the geometry of the tube. The tube is thought to represent entanglements. These should be character-ized by yet another parameter: the distance between these entanglements. If we assume N_e segments between two entanglements, the distance d_e be-tween them is given by the end-to-end distance spanned by these N_e segments (provided they can be represented by a Gaussian chain): $d_e = \sqrt{N_e l^2}$, where l is the segment length. The end-to-end distance of the entire chain is given by $\sqrt{N l^2} = \sqrt{L l}$, where $L = N l$ is the contour length. Let us accomplish a coarse-graining such that the new "segment length" is the entanglement distance d_e. The end-to-end distance must remain the same as before:

$$R_{ee}^2 = Ll = L'd_e \tag{1.68}$$

We define a virtual "thickness" of the new contour length L' (the so-called primitive path), which should be again the end-to-end distance of the seg-ments between two entanglements, d_e. It is an intuitive step to define this thickness as the tube diameter:

$$d \equiv d_e = \sqrt{N_e l^2} \tag{1.69}$$

Given that the tube is a virtual object representing the topological constraints, it is not an obvious one. However, we will show that the introduction of *one* additional length scale is sufficient to obtain a consistent description of the dynamics in long-chain polymer melts.

The dynamics of a chain in a tube described above may be summarized as in Fig. 1.20, which shows schematically the segmental mean square displace-ments versus time in a double logarithmic representation. For times $t < \tau_e$ we expect Rouse behavior, which gives, as already derived above, a power law $\langle r^2(t) \rangle \propto t^{1/2}$ reflecting the sub-Fickian motion due to correlations of dis-placements along the chain away from the probe monomer [see Eq. (1.63)]. In the previous section an incoherent experiment on H-PEP was presented that corroborates this Rouse prediction at short times.

For times $t > \tau_e$ the Rouse dynamics is constricted to the tube, which represents basically a random walk. The mean square displacement can be calculated by first switching to the coordinates $s_n(t)$ along the primitive path of the tube. Then as in Eqs. (1.62) and (1.63) the mean square displacement along the tube profile for $t < \tau_R$ can be calculated:

$$\left\langle [s_n(t) - s_n(0)]^2 \right\rangle = \left(\frac{4k_B T l^2 t}{3\xi\pi} \right)^{1/2} = \left(\frac{4W l^4 t}{9\pi} \right)^{1/2} \tag{1.70}$$
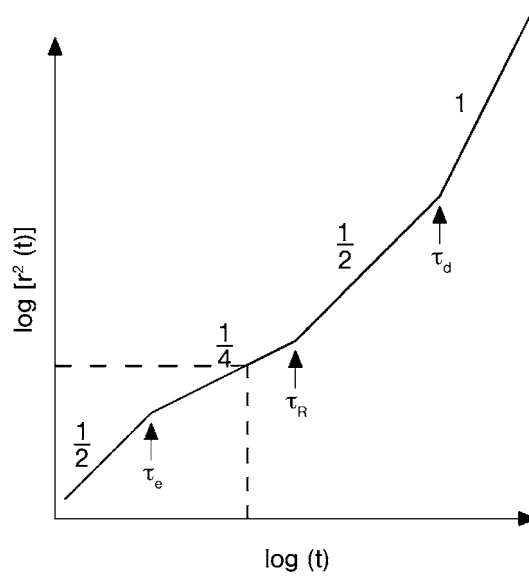
Fig. 1.20 Schematic representation of the segmental mean square displacements versus time in a double logarithmic plot. The white rectangle indicates the time range accessible by NSE spectroscopy.

The factor 1/3 compared to Eq. (1.63) accounts for the fact that the motion is restricted to one dimension. Since the tube is a random walk with step length d, the mean square displacement in three-dimensional real space is given by $\Phi_n = Zd^2 = Ld$, where Z is the number of steps and $L = |s_n(t) - s_n(0)|$ is the contour length of the primitive path:

$$\Phi_n = d\langle|s_n(t) - s_n(0)|\rangle \qquad (1.71)$$

$$= d\big(\langle[s_n(t) - s_n(0)]^2\rangle\big)^{1/2} \qquad (1.72)$$

and with Eq. (1.70) we get[3]

$$\Phi_n = \left(\frac{4k_\mathrm{B}Tl^2d^4t}{3\pi\xi}\right)^{1/4} = \left(\frac{4Wl^4d^4t}{9\pi}\right)^{1/4} \qquad (1.73)$$

If we force the sub-Fickian motion to take place along a random walk, which alone gives rise to a behavior $\langle r^2(t)\rangle \propto t^{1/2}$, it is not surprising that the two $t^{1/2}$ laws finally yield a power law $\langle r^2(t)\rangle \propto t^{1/4}$ in the regime of local reptation.

3) Note that the approximate prefactor of Eq. (6.110) in Doi and Edwards (1986) differs from the exact result given here (Eq. 1.73) by a factor $[4/(3\pi)]^{1/4}$.

For times longer than τ_{R} the dynamics is dominated by center-of-mass diffusion, which gives $\langle r^2(t) \rangle \propto t$. Of course, we have to apply the arguments as for the Rouse motion in the tube, since the center-of-mass diffusion is again forced to take place along the random-walk profile of the tube. This leads to $\langle r^2(t) \rangle \propto t^{1/2}$ for $\tau_{\mathrm{R}} < t < \tau_{\mathrm{d}}$, where τ_{d} is the disentanglement time. Note that this power law is the same as for the Rouse regime ($t < \tau_{\mathrm{e}}$), but for a different reason.

Finally, for times $t > \tau_{\mathrm{d}}$, the chain has escaped completely from the tube and three-dimensional Fickian diffusion can take place, i.e. we expect $\langle r^2(t) \rangle \propto t$.

What is the Entanglement Time τ_{e}?

Since there is quite a bit of confusion in the literature, the definition of τ_{e} deserves its own small subsection. Note that we will imply here and in the following the validity of Eq. (1.69). There are two classical ways of defining this time scale, in addition to the one we shall use in this chapter.

- The first assumes τ_{e} to be the Rouse time τ_{R} of a chain with an end-to-end distance $R_{\mathrm{ee}} = \sqrt{N_{\mathrm{e}}}\, l$, where N_{e} is the number of segments between two entanglements. This τ_{e} refers via τ_{R} to the slowest Rouse mode of a chain with an end-to-end distance R_{ee} fitting into the tube:

$$\tau_{\mathrm{e}}' = \frac{\tau_{\mathrm{R}} N_{\mathrm{e}}^{\,2}}{N^2} = \frac{N_{\mathrm{e}}^{\,2} l^2 \xi}{3\pi^2 k_{\mathrm{B}} T} = \frac{d^4}{\pi^2 W l^4} \tag{1.74}$$

- The second way is also quite evident: τ_{e} is the time when the mean square displacement of a segment equals the tube diameter squared. This definition results by equating Φ with d^2 and adopting τ_{e} in Eq. (1.63):

$$\tau_{\mathrm{e}}'' = \frac{\pi d^4 \xi}{12 k_{\mathrm{B}} T l^2} = \frac{\pi d^4}{4 W l^4} \tag{1.75}$$

This is the definition in Doi and Edwards (1986), after applying the correction mentioned with respect to Eq. (1.63).

- The third definition is the one we will use in this chapter. Combining the time dependence of the mean square displacement as defined within the Rouse model (Eq. 1.63) and that of the reptation model for the local reptation regime (Eq. 1.73), τ_{e} follows by calculating the intersection point of these two straight lines (if plotted as shown schematically in Fig. 1.20). Equating (1.63) and (1.73) finally yields:

$$\tau_{\mathrm{e}} = \frac{\pi d^4}{36 W l^4} \tag{1.76}$$

This point in time marks the transition from free Rouse behavior to restricted motion, and is therefore the best choice for a definition of τ_e. We will use this definition in the following. However, it deviates by just $\approx 15\%$ from the first definition. Note that inserting τ_e in Eq. (1.63) for the Rouse regime or into Eq. (1.73) for the local reptation regime yields a mean square displacement $\Phi_n = d^2/3$ at τ_e.

1.6.1
Validating the Tube Concept on a Molecular Scale

NSE measurements of the self-correlation function have been performed at the NSE spectrometer at the DIDO research reactor FRJ2 in Jülich (Monkenbusch et al. 1997) on a fully protonated PE sample of 0.3–0.4 mm thickness and a molecular weight $M_w = 190$ kg mol^{-1} (Wischnewski et al. 2003). Fig. 1.21 shows the data for $T = 509$ K at $Q = 1$ and 1.5 nm^{-1}.

The total measuring time for each single (Q, t) pair (including background) was $\simeq 5$ h, requiring a very high temporal stability of the instrument. The neutron wavelength of $\lambda = 0.8$ nm allowed for a Fourier time range 0.1 ns $\leq t \leq 22$ ns in the normal instrument setup, and 0.01 ns ≤ 0.13 ns in a special short-time configuration with small precession coils in the sample region. All data shown stem from an integrated detector area of 615 cm^2. The solid lines
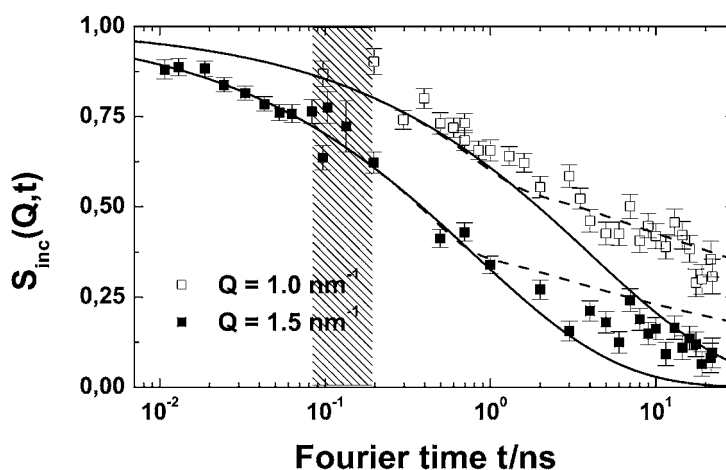
Fig. 1.21 NSE data obtained from the incoherent scattering from a fully protonated PE melt with $M_w = 190$ kg mol^{-1} at $T = 509$ K for $Q = 1.0$ and 1.5 nm^{-1} (Wischnewski et al. 2003). At the range boundaries (shaded gray bar) of the two spectrometer configurations (short or normal, see text), the data quality is worse than the bulk of the data points, as seen by the sizes of the error bars. The solid and dashed lines represent the predictions of Eqs. (1.64) and (1.78), respectively (see text after Eq. 1.78 for more details).

in Fig. 1.21 represent the Rouse prediction . For short times they agree nicely with the experimental data.

For the very long PE chains used here, virtually all of the scattering intensity stems from "inner" segments. These should exhibit the same segmental diffusion behavior, and if the assumption of a Gaussian shape of the diffusive displacement probability distribution holds for all times, the mean square segment displacement can be extracted directly from $S(Q,t)$ as defined in Eq. (1.18):

$$\langle r^2(t) \rangle = -6 \ln[S_{\text{inc}}(Q,t)]/Q^2 \qquad (1.77)$$

Fig. 1.22 displays the H-PE data in this representation.

The mean square displacement in the Rouse regime has been derived in Eq. (1.63). Inserting the previously determined value for the Rouse rate $W(509\,\mathrm{K})l^4 = 7 \pm 0.7$ nm^4 ns^{-1} (Richter et al. 1993) from the analysis of the single-chain structure factor of low-molecular-weight PE melts, Eq. (1.63) is quantitatively corroborated as already seen for the H-PEP data in the last section. Also a transition to a regime $\propto t^{1/4}$ is clearly visible. The crossover time can be extracted from Fig. 1.22 by fitting the data with Eq. (1.63) for the Rouse regime and Eq. (1.73) for the local reptation regime. The only free parameter is then the crossover time, yielding $\tau_e \simeq 1$ ns corresponding to a tube diameter of 3 nm (Eq. 1.76).
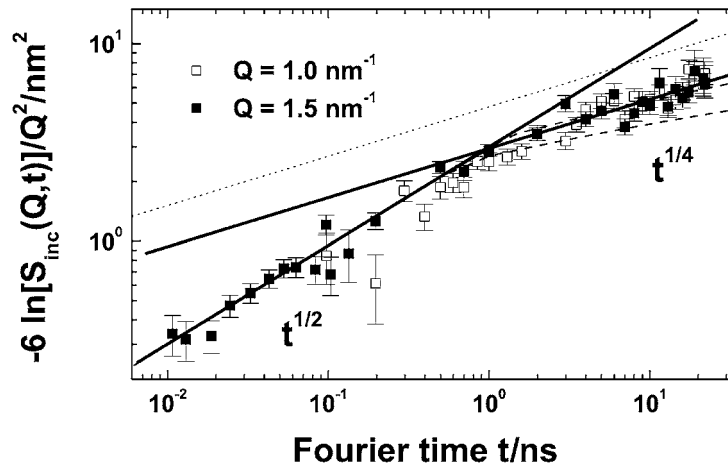
Fig. 1.22 Same data as shown in Fig. 1.21 in a representation of $-6\ln[S_{\text{inc}}(Q,t)]/Q^2$ versus time, i.e. the mean square displacement $\langle r^2(t) \rangle$ as long as the Gaussian approximation holds (Wischnewski et al. 2003). The solid lines describe the asymptotic power laws $\langle r^2(t) \rangle \propto t^{1/2}$ and $t^{1/4}$, respectively; the dotted line results by inserting $d = 4.8$ nm in Eq. (1.73); and the dashed lines represent the prediction of Eq. (1.78) (see text for more details).

On the other hand, this value may be calculated by using Eq. (1.76), where the elementary step length of the Gaussian contorted virtual tube is identified with the tube diameter, which can be extracted from NSE experiments on the pair correlation function. These measurements will be discussed in detail below, but the resulting tube diameter may be anticipated at this point: $d = 4.8$ nm. Equation (1.76) then yields $\tau_e \simeq 7$ ns. The dotted line in Fig. 1.22 results by inserting $d = 4.8$ nm in Eq. (1.73) for the local reptation regime. The intersection with the $\propto t^{1/2}$ line defines $\tau_e = \tau_e = 7$ ns as calculated above.

The apparent strong discrepancy between the crossover time of $\tau_e = 1$ ns with a tube diameter of 3 nm extracted from the incoherent data and the values $\tau_e \simeq 7$ ns and $d = 4.8$ nm from the coherent data will be discussed below.

First, we apply the same evaluation procedure as described above to the H-PEP data, revealing the mean square displacements of H-PEP. They have already been discussed for short times in the last section. Fig. 1.23 displays the results for the entire time range.

Again, a deviation from $\langle r^2(t) \rangle \propto t^{1/2}$ is clearly visible for $t \gtrsim 10$ ns, while the data are in agreement with Eq. (1.63) for $t \lesssim 10$ ns as already shown in the last section. Using $W(492\,\mathrm{K})l^4 = 3.26$ nm^4 ns^{-1} (Richter et al. 1993), the data were fitted with Eqs. (1.63) and (1.73), yielding a crossover time of $\tau_e = 8.4$ ns and a tube diameter of about 4.3 nm.
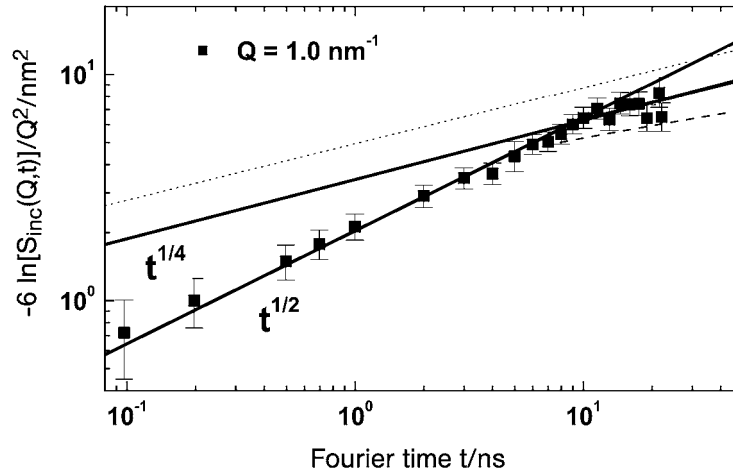
Fig. 1.23 Data of H-PEP in the representation of $-6\ln[S_{\mathrm{inc}}(Q,t)]/Q^2$ versus time for $T = 492$ K (Wischnewski et al. 2003). As before, the solid lines describe the asymptotic power laws; the dotted line results from Eq. (1.73); and the dashed line is from Eq. (1.78) (see text for details).

To compare this result with the tube diameter obtained from the single-chain dynamic structure factor of PEP, again we will anticipate the results of the evaluation discussed in detail below: $d_{\mathrm{PEP}} = 6$ nm, i.e. $[\tau_{\mathrm{e}}] = 40$ ns (see dotted line in Fig. 1.23), again in contradiction to $d = 4.3$ nm and $\tau_{\mathrm{e}} = 8.4$ ns, obtained from an interpretation of the self-correlation data in terms of the Gaussian approximation.

In the derivation of Eq. (1.73), the Gaussian width after a diffusion time t of the single segment distribution along the one-dimensional tube contour, the path coordinate s is taken to be the time-dependent displacement. Projecting this on the Gaussian contorted tube again corresponds to a Gaussian sub-linear diffusion in real space (Eq. 1.73). However, the real process has to be modeled by projecting the segment probability distribution due to curvilinear Rouse motion on the linear coordinate s onto the random-walk-like contour path of the contorted tube, leading to a non-Gaussian probability distribution of the segments at times $t > \tau_{\mathrm{e}}$. The necessity to perform the proper averaging was first shown by Fatkullin and Kimmich (1995) in the context of the interpretation of field-gradient NMR diffusometry data (Fischer et al. 1999), which yield results that are analogous to the incoherent neutron scattering functions. However, they are in another time and space regime covering mainly the regime $\tau_{\mathrm{R}} < t < \tau_{\mathrm{d}}$. Their result

$$S_{\mathrm{inc}}(Q, t > \tau_{\mathrm{e}}) = \exp\left[\frac{Q^4 d^2}{72} \frac{\langle r^2(t) \rangle}{3}\right] \mathrm{erfc}\left[\frac{Q^2 d}{6\sqrt{2}} \sqrt{\frac{\langle r^2(t) \rangle}{3}}\right] \qquad (1.78)$$

invalidates the Gaussian approximation (Eq. 1.64) for times above τ_{e}. We note that Eq. (1.78) is strictly valid only for $t \gg \tau_{\mathrm{e}}$ when $\langle r^2(t) \rangle \gg d^2$. The effect on the scattering function is that, if (wrongly) interpreted in terms of the Gaussian approximation, the crossover to local reptation appears to occur at significantly lower values of τ_{e}.

Figs. 1.21 to 1.23 show a comparison of the scattering function $S_{\mathrm{inc}}(Q, t)$ as predicted by Eqs. (1.64) (Rouse regime) and (1.78) (dashed lines, local reptation regime) with the NSE data. The parameters Wl^4 and d were fixed to the values taken from the single-chain structure factor measurements. For PE and $Q = 1$ nm^{-1}, the free Rouse regime ($t < \tau_{\mathrm{e}}$) as well as the local reptation regime are perfectly reproduced. For $Q = 1.5$ nm^{-1} in the case of PE (lower dashed line in Figs. 1.21 and 1.22) and for $Q = 1$nm^{-1} for PEP, the prediction of Eq. (1.78) lies slightly outside the error band of the data points.

The spatial resolution increases with increasing Q-values. Agreement with theory may only be expected for Q-values less than $2\pi/d$. For the tube diameter of 4.8 nm in PE, the "limiting" wavevector would be 1.3 nm^{-1}, which may explain why deviations become visible at $Q = 1.5$ nm^{-1}. The same holds

for PEP, where, with $d = 6$ nm, the typical wavevector would be about $Q = 1$ nm^{-1}.

Up to now we have considered the segmental mean square displacement in a long-chain polymer melt. Now we will investigate the single-chain dynamic structure factor. As already demonstrated in Section 1.5, the Rouse model does not describe the dynamics of long chains in the melt. After an initial decay of $S(Q, t)$ by a free three-dimensional Rouse motion, the relaxation slows down. We have seen above that this slowing down starts when the mean square displacement of the chain segments becomes comparable to the diameter squared of the virtual tube described in the reptation model. The tube concept provides a model for the pair correlation scattering function of a single chain in the melt. It is given by (de Gennes 1981; Doi and Edwards 1986):

$$\frac{S(Q, t)}{S(Q)} = [1 - F(Q)]S_{\text{locrep}}(Q, t) + F(Q)S_{\text{esc}}(Q, t) \qquad (1.79)$$

Here, $F(Q)$ is the (cross-sectional) form factor of the tube:

$$F(Q) = \exp[-(Qd/6)^2] \qquad (1.80)$$

The two processes that determine the relaxation of a chain in a tube are local reptation and the creeping of the entire chain out of the tube where the chain follows its own profile:

$$S_{\text{locrep}}(Q, t) = \exp(t/\tau_0)\,\text{erfc}\big(\sqrt{t/\tau_0}\big) \qquad (1.81)$$

$$S_{\text{esc}}(Q, t) = \sum_{p=1}^{\infty} \frac{2AN\mu}{\alpha_p^2(\mu^2 + \alpha_p^2 + \mu)} \sin^2(\alpha_p) \exp\left(-\frac{4t\alpha_p^2}{\pi^2\tau_{\text{d}}}\right) \qquad (1.82)$$

where $\mu = Q^2 N l^2 / 12$ and α_p are the solutions of the equation $\alpha_p \tan(\alpha_p) = \mu$; A is a normalization constant, so that $S_{\text{esc}}(Q, 0) = 1$. The two time scales in Eqs. (1.81) and (1.82) are given as follows: the first, $\tau_0 = 36/(Wl^4 Q^4)$, is for Rouse-type segment diffusion along the tube; the second is the so-called disentanglement time $\tau_{\text{d}} = 3N^3 l^2 / (\pi^2 W d^2)$ for reptation-type escape of the chain from the tube (creep).

In the high-Q limit, i.e. $R_{\text{g}}Q \gg 1$, $\alpha_p \approx (p - \frac{1}{2})\pi$ and $S_{\text{esc}}(Q, t)$ in Eq. (1.82) can be approximated by

$$S_{\text{esc}}(Q, t) = \frac{8}{\pi^2} \sum_{p,\text{odd}} \frac{1}{p^2} \exp\left(-\frac{p^2 t}{\tau_{\text{d}}}\right) =: \mu_{\text{rep}}(t) \qquad (1.83)$$

Note that $S_{\text{esc}}(Q, 0)$ is again normalized to unity. In this equation, $\mu_{\text{rep}}(t)$ is called the "tube survival probability" and is directly related to the relaxation
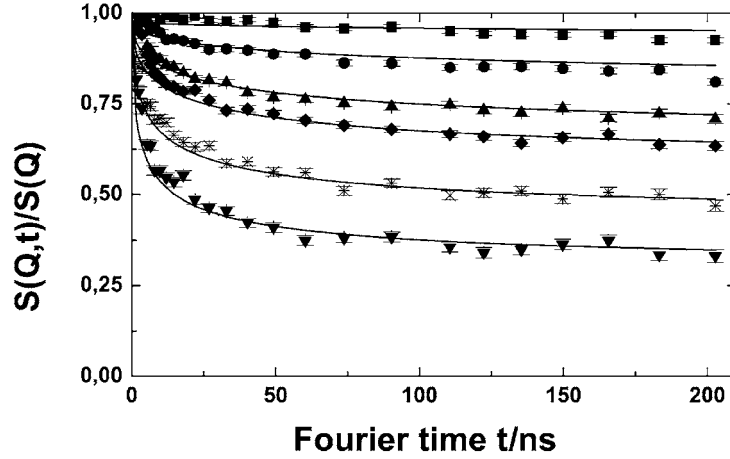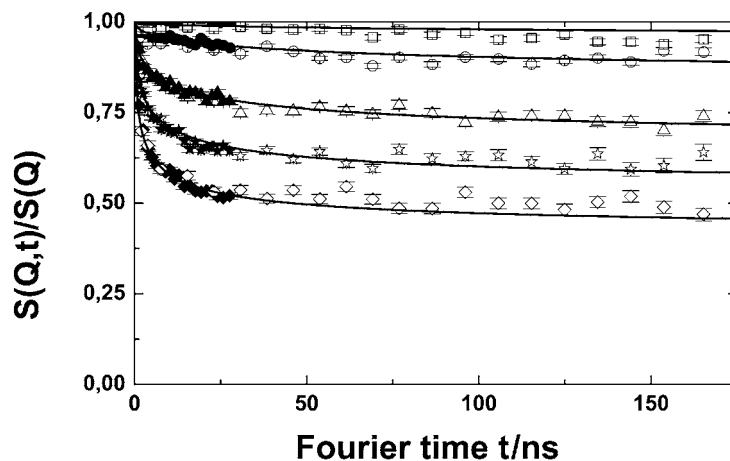
Fig. 1.24 Plot of $S(Q,t)/S(Q)$ from a $M_{\rm w} = 200$ kg mol^{-1} PEP melt at $T = 492$ K for the scattering wavevectors $Q = 0.3$, 0.5, 0.68, 0.77, 0.96, and 1.15 nm^{-1}, from above (Wischnewski et al. 2003). The solid lines represent a fit with Eq. (1.79).

function, $G(t)/G_{\rm e} = \mu_{\rm rep}(t)$, where $G_{\rm e}$ is the plateau modulus. By Fourier transformation of $G(t)$ and replacing the sum in Eq. (1.83) by an integral, it can be shown that, for times $t < \tau_{\rm d}$ or $\omega > \omega_{\rm d} = 1/\tau_{\rm d}$ (Doi and Edwards 1986; Milner and McLeish 1998; McLeish 2002),

$$G''_{\rm rep}(\omega) \propto \omega^{-1/2} \tag{1.84}$$

Now we will describe NSE results from high-molecular-weight PE and PEP samples by the single-chain dynamic structure factor of Eqs. (1.79) to (1.82). Inspecting the formulas we recognize that all the parameters needed can easily be calculated or are already known from the evaluation of NSE data of the respective short-chain systems: the segment length l of PE [$l = 0.41$ nm (Boothroyd et al. 1991)] and PEP [$l = \sqrt{l_0^2 C_\infty n} = 0.74$ nm with $n = 3.86$ the effective bond number per monomer (Richter et al. 1992; Richter et al. 1993)], the Rouse variables [$Wl^4 = 7$ nm^4 ns^{-1} for PE at $T = 509$ K, and $Wl^4 = 3.26$ nm^4 ns^{-1} for PEP at $T = 492$ K (Richter et al. 1993)] and the number of segments [$N = 13\,013$ for the $M_{\rm w} = 190$ kg mol^{-1} PE sample, and $N = 2857$ for the $M_{\rm w} = 200$ kg mol^{-1} PEP sample]. There is only one parameter left that is not known: the diameter of the virtual tube d, representing the topological constraints due to entanglements in long-chain polymer systems. In Eq. (1.69) d was defined as the end-to-end distance of a chain with $N_{\rm e}$ segments, where $N_{\rm e}$ is the number of segments between two entanglements.

Fig. 1.25 Plot of $S(Q,t)/S(Q)$ from a $M_{\mathrm{w}} = 190$ kg mol^{-1} PE melt at $T = 509$ K for the scattering wavevectors $Q = 0.3$, 0.5, 0.77, 0.96, and 1.15 nm^{-1}, from above. The data were taken with a wavelength of the incoming neutrons of $\lambda = 0.8$ nm (filled symbols) and $\lambda = 1.5$ nm (open symbols). Solid lines represent a fit with Eq. (1.79).

Fig. 1.24 shows the NSE data for PEP with $M_{\mathrm{w}} = 200$ kg mol^{-1} at $T = 492$ K (about 10% H-PEP in D-PEP). The data were taken at the IN15 spectrometer (ILL, Grenoble) and corrected for background and resolution. They show a dramatic slowing down of the relaxation after an initial decay. The curves end up in a plateau for all Q-values at high Fourier times, reflecting the topological constraints. The solid lines in Fig. 1.24 represent a fit with Eq. (1.79). As explained above, the only free parameter to fit all Q-values simultaneously is the tube diameter d. The description of the data is excellent over the whole range of Fourier times and Q-values. The resulting diameter is $d = 6$ nm.

Fig. 1.25 shows the results of a comparable measurement for H-PE in D-PE with a molecular weight $M_{\mathrm{w}} = 190$ kg mol^{-1} at $T = 509$ K. Again, the data show the characteristic plateaus at long times for all Q-values, and again the description by the reptation model is excellent having in mind that only one parameter can be varied. The tube diameter for this PE sample is $d = 4.8$ nm. What do we learn from these two experiments?

- The reptation model (Eqs. 1.79 to 1.82) yields an excellent description of the PE and PEP data at high molecular weights over the entire range of Fourier times and scattering vectors. For the fit, only one parameter is free, the tube diameter d, for which we obtain reasonable values ($d = 6$ nm for PEP and $d = 4.8$ nm for PE).
- Calculating the disentanglement time $\tau_{\mathrm{d}} = 3N^3 l^2/(\pi^2 W d^2)$, we obtain $\tau_{\mathrm{d}} = 0.02$ s (with $W = 242$ ns^{-1}) for PE and $\tau_{\mathrm{d}} = 0.01$ s (with $W = 10.9$ ns^{-1}) for PEP. Since the disentanglement time depends on the chain

length to the third power ($\tau_{\mathrm{d}} \propto N^3$) in the accessible NSE time range (some hundreds of nanoseconds), the tube escape term (with a time constant in the range of 10 ms) is virtually constant for the high-molecular-weight samples. In conclusion, the local reptation process dominates the polymer dynamics in the NSE time range for long-chain polymer systems.

- Assuming that S_{esc} is still time-independent in the time window of NSE and that S_{locrep} has essentially decayed to zero in the plateau region, we find from Eq. (1.79) that $S(Q,t) \approx F(Q)$. Therefore reading the plateau values permits the direct extraction of the tube diameter via $\exp(-Q^2 d^2/36)$.

- The initial decay is dominated by Rouse dynamics. We have seen from the incoherent experiments that the segments undergo free Rouse relaxations as long as the mean square displacement is smaller than the tube diameter squared. The Rouse model is not included in Eqs. (1.79) to (1.82)! However, if the fit is restricted to times $t > \tau_{\mathrm{e}}$, the results remain the same. The agreement at times $t < \tau_{\mathrm{e}}$ is somewhat accidental.

What about the slow creep process? As mentioned above, this kind of motion is too slow for NSE, but easily detectable by rheology. Fig. 1.26 shows the loss modulus $G''(\omega)$ versus frequency in a double logarithmic plot. Following Eq. (1.84) for the creep process $G''_{\mathrm{rep}}(\omega) \propto \omega^{-1/2}$ is expected and clearly observed at frequencies higher than the inverse disentanglement time τ_{d}.
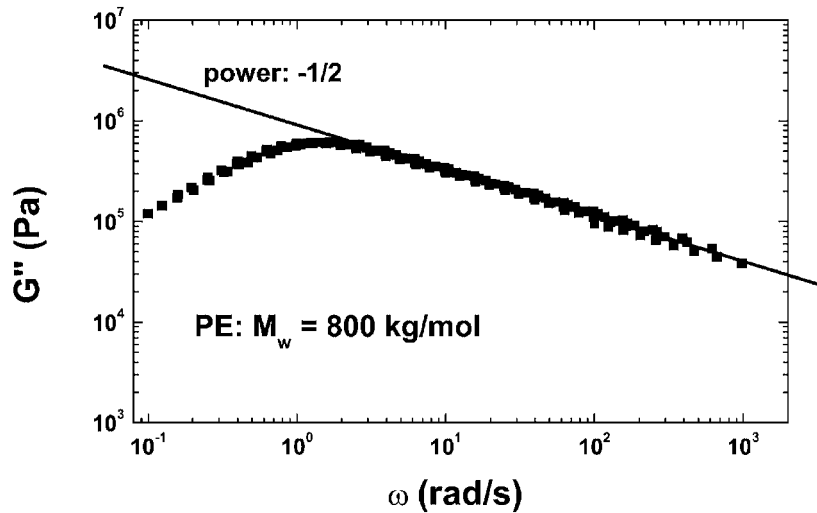
Fig. 1.26 Loss modulus $G''(\omega)$ of polyethylene with $M_{\mathrm{w}} = 800$ kg mol^{-1} (reference temperature $T = 509$ K) measured at the rheometer in Jülich. The solid line illustrates the expectation for the creep process at frequencies higher than the peak frequency ω_{d} (Eq. 1.84).

Is Everything Fine?

We have shown above that the dynamics in polymer melts is determined by a balance of viscous and entropic forces. A thermally activated fluctuation may be envisaged as a slightly stretched chain. The entropy tries to bend the chain back but has to battle against friction. This dynamics is described in the Rouse model, representing the environment of a test chain by a heat bath that causes thermal activation.

Another approach to the chain dynamics is the mean square displacement Φ_n of a chain segment. Due to the fact that one test segment n is linked to other segments, Φ_n can be described by a sub-Fickian diffusion; the respective time dependence is predicted in the framework of the Rouse model to be proportional to $t^{1/2}$. Both the predicted relaxational structure factor of a labeled test chain as well as the segment mean square displacement have been corroborated by NSE experiments: the former by analyzing the single-chain dynamic structure factor obtained by measuring a few labeled chains in a deuterated matrix for different Q-values, and the latter by an incoherent NSE experiment on fully protonated polymers addressing the self-correlation function. As long as the Q-value is not too high, i.e. we do not observe local details of a segment, and as long as the chains are short, so that they do not entangle (or the time is short enough that they do not know that they are entangled), the Rouse model gives an excellent description of the short-time dynamics in polymer melts.

When the chains become longer, topological chain–chain interactions come into play. We have shown above that the concept of a virtual tube representing the entanglements is very successful in describing the dynamics of long-chain systems. This holds again for the single-chain dynamic structure factor, showing characteristic plateaus at long times where further relaxation is hindered due to topological constraints. Here the reptation model gives a perfect description of the structure factors over the entire range of times and Q-values and allows us to extract the diameter of the virtual tube as the only free parameter of the model. This also holds for the segmental mean square displacement, where the tube concept predicts a transition from a power law $\propto t^{1/2}$ to $\propto t^{1/4}$ at a time constant τ_e. This has indeed been observed for polymers in incoherent NSE experiments addressing the self-correlation function. After a proper evaluation and taking into account non-Gaussian effects in the local reptation regime, the extracted tube diameter is in quantitative agreement with the results from the single-chain dynamic structure factor.

Finally, though not observable in NSE, it has been shown that the slow creep process is traceable in high-molecular-weight polymer melts by analyzing the loss modulus $G''(\omega)$.

This would be the last page of this chapter about polymer dynamics if there were not some observations that are difficult to understand just adopting

Rouse and reptation theory. A few of the many known examples may be listed here:

- The viscosity η in the reptation regime is expected to be proportional to the longest relaxation time. In the reptation concept, this time is the disentanglement time $\tau_{\mathrm{d}} \propto M^3$. Therefore, $\eta \propto M^3$ is anticipated. It has been known for a long time that the $\eta \propto M^3$ dependence is reached only at very high molecular weights, but there exists an intermediate range of molecular weights, where, though the polymer melt is in the well-entangled regime, a power law $\eta \propto M^{3+\alpha}$ with $\alpha \approx 0.4$ is found. Furthermore, it is known from rheological data that the same holds for the disentanglement time τ_{d}, which in polyisoprene has recently been found to be $\tau_{\mathrm{d}} \propto M^{3.32}$ with a transition to an M^3 dependence at very high molecular weights (Abdel-Goad et al. 2004).

- As derived in Section 1.5, we can write $\Phi_{\mathrm{D}}(\tau_{\mathrm{d}}) = 6D\tau_{\mathrm{d}} \propto Nl^2$ and so, with $\tau_{\mathrm{d}} \propto N^3$ for the diffusion coefficient, $D \propto 1/N^2$. Therefore, for long-chain polymers we expect $D \propto M^{-2}$ following the reptation model. In polybutadiene, Lodge (1999) found $D \propto M^{-2.3}$

- Finally, and in contrast to what has been presented in Fig. 1.26 for high-molecular-weight polyethylene, in polyisoprene (PI), for example, it has been found that the loss modulus exhibits a -0.25 power-law dependence at frequencies $\omega > \omega_{\mathrm{d}}$ (Abdel-Goad et al. 2004), indicating the existence of additional relaxation processes (McLeish 2002; Likhtman and McLeish 2002). This is illustrated in Fig. 1.27. Note that the total molecular weight of this polyisoprene sample ($M_{\mathrm{w}} = 1000 \ \mathrm{kg \ mol^{-1}}$) is higher than that of the PE sample presented in Fig. 1.26. However, the number of entanglements $Z = N/N_{\mathrm{e}}$ is higher for PE ($Z_{\mathrm{PE}} \approx 400$) than for PI ($Z_{\mathrm{PI}} \approx 170$).

It was proposed some time ago that, in addition to the relaxation processes described in the Rouse and reptation theories, there should exist additional degrees of freedom. The main reason for this is the fact that the polymer chains have a finite length. Starting with a chain that is confined in a tube for time $t = t_0$, one may wonder if at a time $t = t_1$ chain segments close to the "open ends" of the tube are as confined as the center part of the chain. Furthermore, it is obvious that not only the test chain itself relaxes but also all chains in the environment that are building the tube: the tube itself is not a fixed object in time!

The former effect – contour length fluctuations (CLF) – will be explored and discussed in the next section; the latter one – constraint release (CR) – will be taken up after that.
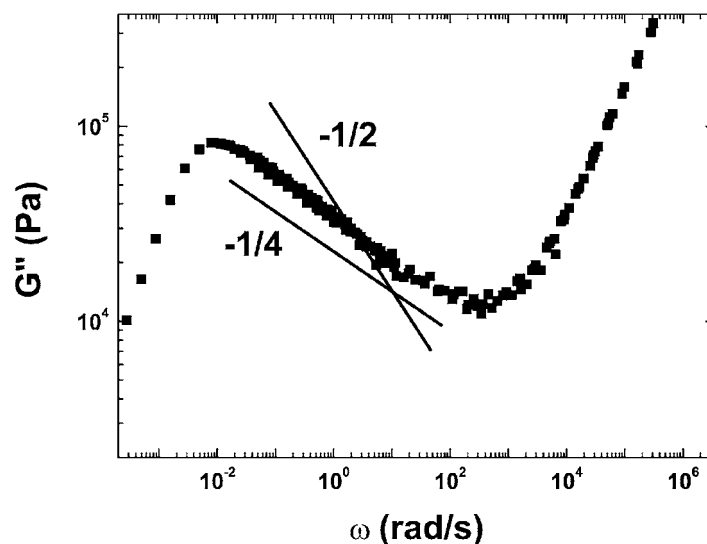
Fig. 1.27 Loss modulus $G''(\omega)$ of polyisoprene with $M_\mathrm{w} = 1000$ kg mol^{-1} at a reference temperature $T = 300$ K measured at the rheometer in Jülich (Abdel-Goad et al. 2004). Figure taken from Wischnewski et al. (2004).

1.7
Limiting Mechanisms for Reptation I: CLF

The finite length of a chain plays an important role due to the existence of chain ends. Their influence is more pronounced in polymer melts of intermediate chain length than in very long-chain systems where the relative weight of the end segments is negligible compared to the total number of segments. We have seen that for PE with $M_\mathrm{w} = 190$ kg mol^{-1} the reptation model gives an excellent description of the single-chain dynamic structure factor. We have also seen that the resulting tube diameter is in agreement with the value extracted from measurements of the segment mean square displacement. Obviously we are in the long-chain limit for the PE system with $M_\mathrm{w} = 190$ kg mol^{-1}. To investigate systematically the chain-length dependence of the chain dynamics, we have measured a series of PE samples with $M_\mathrm{w} = 36, 24.7, 17.2, 15.2$, and 12.4 kg mol^{-1} (Wischnewski et al. 2002).

The experiments were performed at the IN15 spectrometer at the ILL, Grenoble, at $T = 509$ K. The experimental results were corrected for background and resolution. Fig. 1.28 displays the spectra obtained for different molecular weights. The Q-values correspond to: $Q = 0.03$ Å^{-1} (squares), 0.05 Å^{-1} (circles), 0.077 Å^{-1} (triangles up), 0.096 Å^{-1} (diamonds), 0.115 Å^{-1} (triangles down), and 0.15 Å^{-1} (crosses). Filled symbols refer to a wavelength of the incoming neutrons $\lambda = 0.8$ nm, and open symbols to $\lambda = 1.5$ nm.
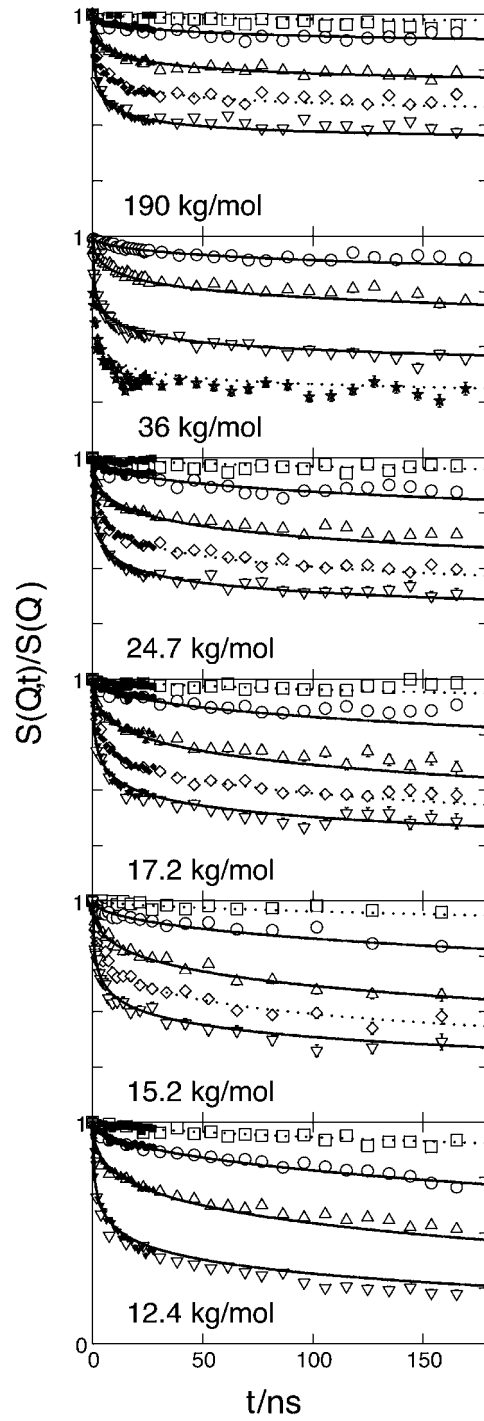
Fig. 1.28 NSE spectra from PE melts of various M_w (see text) (Wischnewski et al. 2002).

For the highest molecular weight $M_\mathrm{w} = 190$ kg mol^{-1} and also for $M_\mathrm{w} = 36$ kg mol^{-1} the spectra are characterized by an initial fast decay reflecting the unconstrained dynamics at early times followed by local reptation and finally very pronounced plateaus of $S(Q, t)$ at later times signifying the tube constraints. The plateau values for the two samples are practically identical.

Inspecting the results for smaller M_w, we realize that: (1) the dynamic structure factor decays to lower values (at $Q = 1.15$ nm^{-1} the value is ≈ 0.5 for $M_\mathrm{w} = 190$ kg mol^{-1}, ≈ 0.4 for $M_\mathrm{w} = 24.7$ kg mol^{-1}, and nearly 0.2 for $M_\mathrm{w} = 12.4$ kg mol^{-1}); and (2) the long-time plateaus start to slope more and more the smaller M_w becomes, with $M_\mathrm{w} = 12.4$ kg mol^{-1} nearly losing the two-relaxation-step character of $S(Q, t)$. Obviously the chain is disentangling from the tube and constraints are successively removed.

Without any theory we can conclude that the spectra change depending on the molecular weight in the sense that the decay of $S(Q, t)$ is stronger and the plateaus are not that pronounced for lower molecular weights. Thereby we have to keep in mind that even the lowest-molecular-weight chain with $M_\mathrm{w} = 12.4$ kg mol^{-1} and $N = 849$ still exhibits $N/N_\mathrm{e} \approx 6$ entanglements (following Eq. 1.69, $N_\mathrm{e} = d^2/l^2 = 4.8^2$ nm^2/0.17 nm$^2 = 136$).

Now we will analyze the data quantitatively using the reptation model (Eqs. 1.79 to 1.82). This is demonstrated in Fig. 1.29, where the solid lines show the result for the lowest ($M_\mathrm{w} = 12.4$ kg mol^{-1}) and the highest ($M_\mathrm{w} = 190$ kg mol^{-1}) molecular weight. The tube diameter is again the only free parameter. For $M_\mathrm{w} = 12.4$ kg mol^{-1}, the tube diameter is significantly larger than for the long-chain melt (see Fig. 1.29, $d(M_\mathrm{w}{=}12.4\,\mathrm{kg\,mol}^{-1}) = 6.0$ nm, $d(M_\mathrm{w}{=}190\,\mathrm{kg\,mol}^{-1}) = 4.8$ nm), reflecting a reduction of the topological constraints. The dotted lines in the lower part of Fig. 1.29 result from the assumption of a constant $d = 4.8$ nm inserted in the reptation model; it is obvious that this significantly underestimates the amount of relaxation in the low-molecular-weight sample. The data for all molecular weights were evaluated by fitting them with the reptation model. All the parameters were kept constant except for the tube diameter. Table 1.1 shows the resulting d.

Tab. 1.1 Tube diameters for different molecular-weight PE melts as obtained by a fit with the reptation model.

| M_w (kg mol^{-1})	d (nm)
190	4.8
36	4.6
24.7	5.4
17.2	5.3
15.2	5.4
12.4	6.0
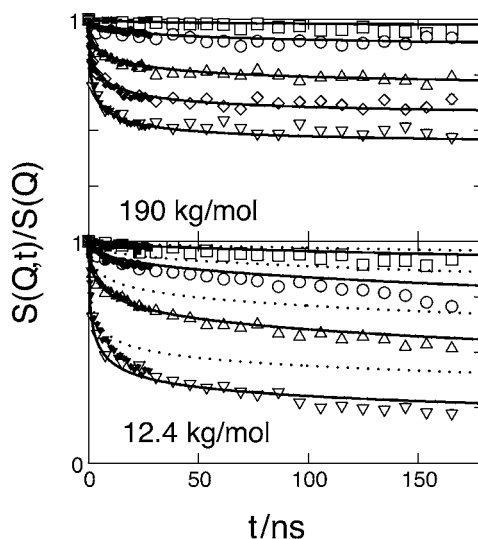
Fig. 1.29 PE data for $M_{\mathrm{w}} = 190$ and 12.4 kg mol^{-1} (Wischnewski et al. 2002). Solid lines represent a fit with the reptation model yielding $d(M_{\mathrm{w}}{=}190\,\mathrm{kg\,mol}^{-1}) = 4.8$ nm and $d(M_{\mathrm{w}}{=}12.4\,\mathrm{kg\,mol}^{-1}) = 6.0$ nm. For the dotted lines, the tube diameter was fixed to 4.8 nm.

The significant increase of the tube diameter with decreasing molecular-weight samples is puzzling. There is no doubt that the reptation picture requires a constant tube diameter as long as the chains are in the well-entangled regime, which is the case for our samples. It is evident, in particular considering the worse fit quality at low molecular weights, that the relaxation is determined not only by reptation but also by an additional process that leads to an *apparently* increasing tube diameter with decreasing molecular weight. As long as we stick to the assumption of a fixed tube, it is also evident that, since for the inner segments there is no difference for a long or short chain, this has to be related to the different relative weight of the chain ends with respect to the total length of the chain.

It is known from broad crossover phenomena, like the molecular-weight dependence of the melt viscosity, that limiting mechanisms exist which affect the confinement and thereby limit the reptation process (Doi and Edwards 1986). Contour length fluctuations (CLF) were proposed as one candidate for such processes. The idea is quite simple. The chain ends undergo the same Rouse-like fluctuations as the inner segments. For an end segment, this leads to the effect that at a given time it may be immersed a bit into the tube. When the segment comes out again, it may have a different direction, not aligned to the original tube curvature. In other words, when one chain end is immersed in the tube, the part of the tube that is not occupied is lost, so the effective
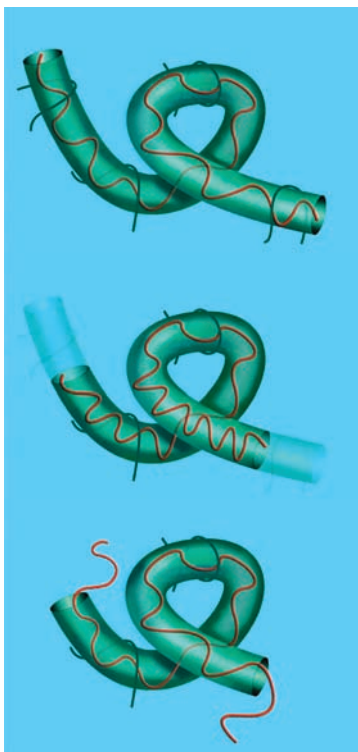
Fig. 1.30 Schematic illustration of contour length fluctuations. Rouse-like motions of end segments lead to the effect that, at a given time, the chain ends are immersed into the tube (central picture). The part of the tube that is not occupied is lost. When they come out again, they may have a different direction, not aligned to the original tube curvature.

tube becomes shorter. The fluctuating chain ends lead to a *time-dependent effective tube length*, i.e. to decreasing constraints with increasing time. This is illustrated in Fig. 1.30.

If we recall the creep process, it is evident that the two relaxation processes are somewhat competitive. Both describe the escape of the chain from the tube confinement: one by diffusion along the tube profile, and the other by destruction of the tube starting from both ends. For times shorter than the Rouse time, which following Eqs. (1.48) and (1.58) is given by $\tau_R = N^2/(\pi^2 W)$, it was recently shown that the effect of reptation on escape from the tube is negligible in comparison to tube length fluctuations (Likhtman and McLeish 2002). This time range corresponds to the times that are accessed in our experiment. Even for the shortest chain $M_w = 12.4$ kg mol^{-1} we get $\tau_R \approx 300$ ns, which is more than the maximum time reached by the high-resolution IN15 NSE spectrometer. This means that for all the NSE

experiments we have to consider CLF rather than the creeping process. In this regime the fraction of monomers released from the tube due to contour length fluctuations has a very simple form:

$$\Psi(t) = \frac{1.5}{Z} \left(\frac{t}{\tau_{\mathrm{e}}} \right)^{1/4} \tag{1.85}$$

where $Z = N/N_{\mathrm{e}}$ is again the number of entanglements per chain.

It is straightforward to show that the scaling with t and Z in Eq. (1.85) emerges exactly from the properties of a linear Rouse chain in a tube. In fact, all the approaches to contour length fluctuations so far (Doi and Edwards 1986; des Cloizeaux 1990) predict for $t < \tau_{\mathrm{R}}$ a simple expression for $\Psi(t)$ like Eq. (1.85) but with different prefactors (≈ 1.2 by Doi and Edwards, and 0.67 by des Cloizeaux). The discrepancy is explained by the different mathematical approximations used. A series of carefully designed one-dimensional stochastic simulations solved the first passage problem for the single Rouse chain in a tube, by taking the limit of the time step tending to zero and the number of monomers going to infinity. These simulations confirmed Eq. (1.85) and gave a result for the prefactor of 1.5 ± 0.02 (Likhtman and McLeish 2002). Without discussing the details, we point to the fact that taking into account the contour length fluctuations for the calculation of the mechanical relaxation functions reproduces the -0.25 power-law dependence in the loss modulus as presented in Fig. 1.27 for chains with not too high numbers of entanglements Z (Likhtman and McLeish 2002).

To incorporate this result in the structure factor calculations, the approximate approach of Clarke and McLeish (1993) was used. We assume that after time t all monomers between 0 and $s(t)$ and between $1 - s(t)$ and 1 have escaped from the tube, where $s(t) = \Psi(t)/2$. Note that here $s(t)$ is a non-dimensional variable between 0 and 0.5, while $s(t)L$ is a section of the contour length following the profile of the primitive path.

This statement contains two approximations: first it assumes that the fraction of the chain that escapes from the tube is the same from each end of the chain, and second it ignores distributions of $s(t)$, replacing it by the single average value. If we make these two assumptions, the rest of the calculation is straightforward. We first use the fact that $R(s,t)$ is a Gaussian variable and therefore

$$\big\langle \exp[\mathrm{i}Q(R(s,t) - R(s',0))] \big\rangle$$

$$= \exp\left[-\tfrac{1}{2} \sum_{\alpha=x,y,z} Q_\alpha^2 \big\langle [R_\alpha(s,t) - R_\alpha(s',0)]^2 \big\rangle \right] \tag{1.86}$$

and then we note that

$$\left\langle [R_\alpha(s,t) - R_\alpha(s',0)]^2 \right\rangle$$

$$= \frac{dL}{3} \begin{cases} |s - s'| & \text{for } s(t) < s < 1 - s(t) \text{ or } s(t) < s' < 1 - s(t) \\ |2s(t) - s - s'| & \text{for } s < s(t) \text{ and } s' < s(t) \\ |2 - s - s' - 2s(t)| & \text{for } s > 1 - s(t) \text{ and } s' > 1 - s(t) \end{cases} \quad (1.87)$$

where $L = Zd$ is the contour length. Replacing the summation in the dynamic structure factor (Eq. 1.11) in Section 1.3.1 by integration, we get

$$S_{\text{esc}}(Q,t) = \int_0^1 \mathrm{d}s \int_0^1 \mathrm{d}s' \, \exp(-2\mu|s - s'|)$$

$$+ 2\int_0^{s(t)} \mathrm{d}s \int_0^{s(t)} \mathrm{d}s' \, \{\exp[-2\mu(2s(t) - s - s')]$$

$$- \exp(-2\mu|s - s'|)\} \quad (1.88)$$

where again $\mu = Q^2 N l^2 / 12$. The integrals can be easily evaluated and we obtain

$$S_{\text{esc}}(Q,t)$$
$$= \frac{N}{2\mu^2}[2\mu + \mathrm{e}^{-2\mu} + 2 - 4\mu s(t) - 4\,\mathrm{e}^{-2\mu s(t)} + \mathrm{e}^{-4\mu s(t)}] \quad (1.89)$$

The lines in Fig. 1.28 were obtained by fitting the data with Eqs. (1.79) to (1.81) and adding instead of the creep term (Eq. 1.82) the above-derived expression for CLF (Eq. 1.89). A group of three common Q-values for all molecular weights is displayed by solid lines to facilitate an easy comparison of the molecular-weight dependence of the curves. Additional Q-values only available for some M_w values are represented by dotted lines.

If we compare the experimental spectra with the model prediction, we generally find good agreement. The gradually increasing decay of $S(Q,t)$ with decreasing M_w is described very well with respect to both the magnitude of the effect and the shape of $S(Q,t)$. We further note that, in particular for smaller M_w, the weighted error between fit and data is significantly smaller compared to the fit with the pure reptation model.

Fig. 1.31 compares the tube diameters as obtained from the fit with the reptation model (Table 1.1) and obtained by replacing the creep term by the
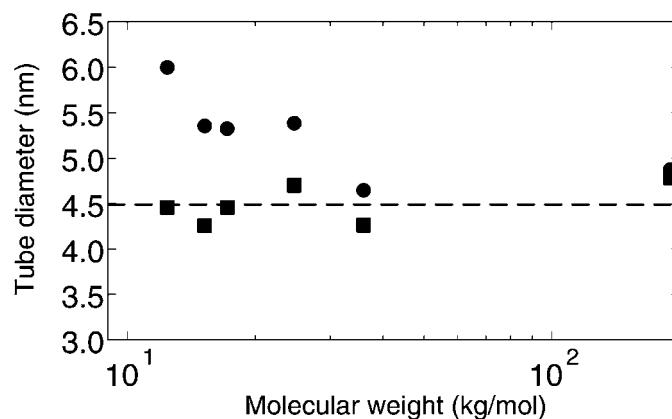
Fig. 1.31 Tube diameters for PE samples with different molecular weights: from pure reptation fit (circles); and when the creep term is replaced by the expression for contour length fluctuations (squares).

concept of contour length fluctuations. At the highest molecular weight, contour length fluctuations are insignificant and both lines of fit yield the same d. At $M_{\mathrm{w}} = 36$ kg mol^{-1}, a slight difference appears, which increases strongly with decreasing length. At $M_{\mathrm{w}} = 12.4$ kg mol^{-1}, the difference in the fitted tube diameters between the two approaches rises to nearly 50%, emphasizing the strong effect of the contour length fluctuation in loosening the grip of the entanglements on a given chain.

However, the main point is that, in contrast to the significant increase of d with decreasing M_{w} if pure reptation is assumed, if CLF is included the tube diameter stays constant. It is important to note that CLF has been included without introducing any new parameter. The data are described over the entire range of time, Q-values, and molecular weights with one single parameter, the tube diameter d.

Thus, the comparison between the experimental chain-length-dependent dynamic structure factor and theoretical predictions clearly shows that, in the time regime $t \leq \tau_{\mathrm{R}}$, contour length fluctuations are the leading mechanism that limits the chain confinement inherent to the reptation picture. Even for chain lengths corresponding to only ≈ 6 entanglements, the tube diameter appears to be a well-defined quantity, assuming the same value as for asymptotically long chains. The confinement is lifted from the chain ends inwards, while the chain center remains confined in the original tube.

To conclude this section we underline the consequences of CLF for the macroscopic properties of polymer melts.

1. Since the structure factor $S_{\mathrm{esc}}(Q,t)$ is directly related to the tube survival probability function $\mu_{\mathrm{rep}}(t)$ (Eq. 1.83) and therefore to the relaxation function, it is evident that the modifications of $S_{\mathrm{esc}}(Q,t)$ as described in this section are reflected in a different ω dependence of $G''(\omega)$. It has been shown that CLF introduces an $\omega^{-1/4}$ regime into the spectrum of the loss modulus. In fact, this power law has already been illustrated in Fig. 1.27 for polyisoprene.

2. The power law for chain diffusion, which has been found to deviate from the prediction of the reptation model, as well as the observed exponent of $3+\alpha$ with $\alpha \approx 0.4$ for the molecular-weight dependence of the viscosity are attributed to the CLF (Doi and Edwards 1986; McLeish 2002).

It is the virtue of the NSE experiments that they provided the first experimental proof of the CLF mechanism quantitatively and on a microscopic scale in space and time.

1.8
Limiting Mechanisms for Reptation II: CR

Up to now we have made a crude approximation by assuming that the topological confinement represented by a virtual tube is constant in time. The basic message of the tube concept is that the confinement that a test chain (e.g. a labeled one) experiences can be represented by a tube built by the adjacent chains. The choice of the test chain is arbitrary, and we assume that the dynamics of all chains in the system is the same (at least as long as we consider one-component systems with a narrow distribution of molecular weights). Having this in mind, it is evident that the tube itself is in motion and the respective constraints possess a finite lifetime. For the effect of contour length fluctuations, which leads to a time-dependent effective tube length, it was sufficient to account for the dynamics of the test chain, because CLF is an escape mechanism of one single chain. There is no need to move away from the single-chain picture and, as we have seen above, there is not even a need to introduce any new parameter. In contrast to CLF, the fact that constraints for the test chain are time-dependent is still true if we freeze the test chain: after some time, reptation or CLF of all the other chains would lead to an effectively free test chain. Here, we have left the single-chain picture and arrived at the more complicated many-chain problem.

In the past decades quite a number of concepts have been developed to account for this additional relaxation process, called "constraint release" (CR). One idea was introduced by Graessley and Struglinski (1986). The lifetime of each constraint building a tube is of the order of the disentanglement time τ_{d}.

If a constraint is released, the tube can move locally. This leads to a Rouse-like motion of the tube itself. In the calculation of the stress relaxation function $G(t)$, this Rouse relaxation of the tube can be accounted for by an additional relaxation function of the Rouse type with time constant τ_d. It turns out, on calculating the reptation part and this additional factor, that the relaxed stress is of the same order of magnitude (in the limit of very long chains). This led to the idea to account for CR by introducing the reptation part squared in the relaxation function. The concept was denoted as "double reptation". In the double reptation concept only one relaxation time was used to describe the constraint release (CR) effect, an oversimplification that has to be adjusted by replacing τ_d by a distribution of relaxation times representing the lifetimes of constraints. It is evident that it makes a difference if the constraint for a test chain is built by the end or the middle part of an adjacent chain.

A self-consistent theory that takes into account the distribution of relaxation times or mobilities for different chain segments has been introduced by Rubinstein and Colby (1988). Likhtman and McLeish (2002) used this formalism to simulate the contribution of constraint release, $R(t)$, to the stress relaxation function. One additional factor (c_ν) to adjust the strength of CR was introduced. Their calculation shows that for times $t < \tau_R$ the relaxation by CR is similar to the relaxation by CLF [$1 - \Psi(t)$ with $\Psi(t)$ as defined in Eq. (1.85)]. In fact, one obtains $R(t)$ by replacing the prefactor in Eq. (1.85) and including c_ν:

$$R(t) = 1 - \frac{1.8}{Z} \left(\frac{c_\nu t}{\tau_e} \right)^{1/4} \tag{1.90}$$

For times longer than the Rouse time, $R(t > \tau_R)$ is described by the lateral relaxation of the tube, which again is considered as a Rouse chain, but with a significantly longer characteristic relaxation time than τ_R. Altogether, the relaxation is determined by five processes. For short times, Rouse modes inside the tube dominate; and for longer times, local reptation (longitudinal modes with a wavelength longer than the tube diameter d) starts to play a role. The escape of the chain from the tube is dominated either by CLF at times $t < \tau_R$ or by reptation for $t > \tau_R$. In the same time regime CR also contributes significantly to the relaxation spectrum. Likhtman and McLeish (2002) achieved a consistent description of experimental rheological data by applying the relaxation function in Eq. (1.90) for the CR mechanism.

Fig. 1.32 shows the calculated effect of all relaxation processes on the loss modulus $G''(\omega)$. The dotted line shows the prediction for pure reptation and Rouse modes. Here, a power law of $-1/2$ in the reptation regime (see Eq. 1.84) and a power of $+1/2$ in the high-frequency Rouse regime are predicted. Taking into account the relaxation by CLF results in the dashed line. Note the change to a $\propto \omega^{-1/4}$ behavior at frequencies above the pure reptation regime, i.e. for
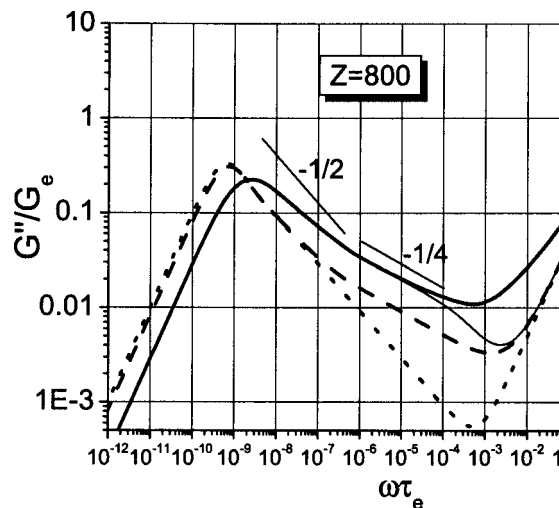
Fig. 1.32 Calculated contributions to $G''(\omega)/G_e$ for a polymer with $Z = 800$ entanglements (Likhtman and McLeish 2002). G_e is the plateau modulus. Lines: pure reptation and Rouse modes (dotted line); adding relaxation by CLF (dashed line); adding relaxation due to CR effect (thin solid line); calculation with all contributions (thick solid line) (see text for further explanation). Figure courtesy of A. E. Likhtman and T. C. B. McLeish.

$\omega > 1/\tau_R$. Adding the relaxation due to the CR effect yields the thin solid line. Finally, the thick solid line illustrates the result of a calculation with all contributions to the relaxation function, including the longitudinal modes.

It may be anticipated at this point that a description of CR on a microscopic scale, i.e. the contribution of CR to the dynamic structure factor as measured by means of NSE, is not available. It is doubtful if this "many-chain" problem can be accounted for in the framework of the quite simple "single-chain" and tube concept. However, is there any chance of observing the CR relaxation on a microscopic scale? Yes, that can be done! We study by NSE a labeled chain in matrices with different chain lengths. The test chain is always the same, but the adjacent chains, which build the constraints of the test chain, have different lengths, i.e. different capabilities to build the tube. One could also say the time scale for the tube will vary with the matrix chain length.

What do we expect? A long chain in a matrix of the same molecular weight will show the well-known plateaus at high Fourier times, as the dynamics is dominated by the local reptation process in the time window of NSE. With decreasing molecular weight of the matrix chains, we expect a faster relaxation of the test chain because the shorter chains build topological constraints with shorter lifetimes. Finally, for very short matrix chains we expect pure Rouse behavior for the long test chain since the adjacent chains cannot build any tube.
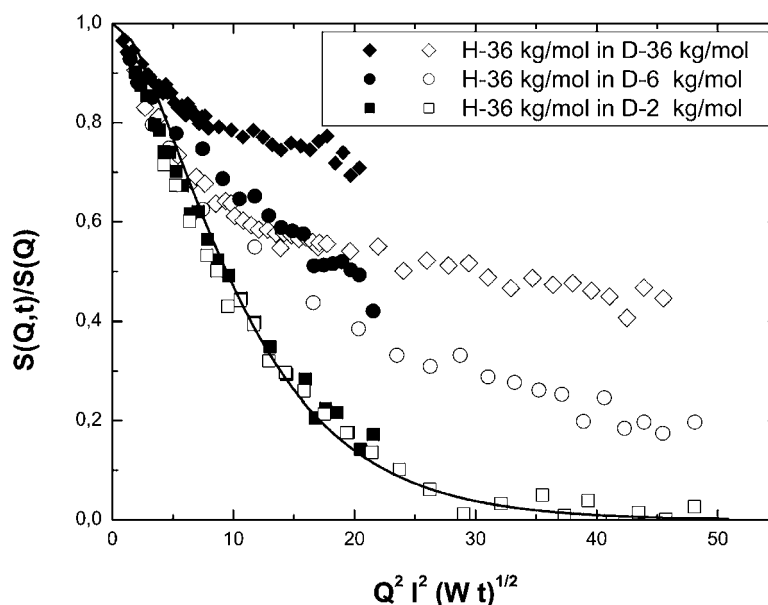
Fig. 1.33 Plot of $S(Q, t)/S(Q)$ measured by NSE (IN15, Grenoble) in a Rouse scaling plot for a protonated test chain with $M_\mathrm{w} = 36$ kg mol^{-1} in a deuterated matrix of 36, 6, and 2 kg mol^{-1} each for two Q-values: 0.77 nm^{-1} (filled symbols), and 1.15 nm^{-1} (open symbols). The solid line represents a fit with the Rouse model for the sample with a 2 kg mol^{-1} matrix (Zamponi 2004).

Fig. 1.33 shows the result of such an experiment. It depicts the NSE data of three samples. The test chain is a protonated PE chain with $M_\mathrm{w} = 36$ kg mol^{-1}. The matrix is varied between $M_\mathrm{w} = 36$ and 2 kg mol^{-1}. The dynamic structure factor is represented in a Rouse scaling as introduced in Section 1.5.1. In this representation, Rouse curves fall on one master curve for different Q-values. For clarity, only two different Q-values are shown for each sample: $Q = 0.77$ nm^{-1} (filled symbols) and 1.15 nm^{-1} (open symbols). For the 2 kg mol^{-1} matrix the dynamic structure factors merge onto one master curve for the two different Q-values. This holds also for other Q-values that are not shown. The dynamic structure factor is very close to the Rouse expectation, though the friction coefficient (the solid line represents a fit with the Rouse model) is higher than expected for a monodisperse 2 kg mol^{-1} sample by a factor of about 2. Note that in this experiment a long chain with a molecular weight of 36 kg mol^{-1} behaves in a Rouse-like way because the short matrix chains are not able to build a tube! The two samples with longer matrix chains show the typical splitting for the two presented Q-values. Furthermore, it is obvious that the relaxation is significantly faster for the sample with the 6 kg mol^{-1} matrix compared to the monodisperse system of proto-

nated 36 kg mol^{-1} chains in a deuterated 36 kg mol^{-1} matrix due to the onset of the CR effect.

The NSE data show clearly the effect of CR. However, we abstain from the introduction of theoretical concepts that could describe the data by means of an oversimplified phenomenological "ad hoc" assumption. It is possible, for instance, to get a satisfactory description of the NSE data by multiplying a tube – Rouse – structure factor with the known reptation structure factor. This adds at the same time a free parameter to the theory, the Rouse time of the tube. However, the significance of such a model is not very strong. Additional degrees of freedom may always be accounted for by some kind of Rouse function, if an additional parameter to be varied is provided. We may at this point stay with the experimental observation of CR, and with the fact that a quantitative description is lacking.

It is probably not a coincidence that, with the description of these obvious limits of the quite simple tube model and its modifications to account for higher-order relaxation processes, we have also reached the end of this chapter about polymer dynamics. A short summary and outlook is given in the next and last section.

1.9
Summary and Outlook

In the previous sections we have tried to develop a consistent picture of the mesoscopic chain dynamics in polymer melts. The systems were always limited to linear homopolymers, the simplest architecture and the simplest chemical composition in this class of soft matter systems.

We started with the dynamics at very short times and demonstrated that in this time regime the segments do not know if they are part of a long entangled system or of a short chain system. This leads to the fact that the dynamics of these two extreme cases cannot be discriminated at very short times. The Rouse model gives a satisfactory description of the segmental motion in this time regime. It is based on the assumption that fluctuations of the observed test chain are activated by a heat bath and that the relaxation of these fluctuations is balanced by viscous forces due to friction and entropic forces. In addition to the internal modes, the chain can undergo a diffusion which is sub-Fickian due to the correlation of different segments within a chain. If the static parameters of the chain are known (segment length, molecular weight), the Rouse model needs only one parameter, namely the effective segmental friction coefficient, to describe the single-chain dynamic structure factor over a wide range of Q-values and Fourier times. It also predicts the time dependence of the segmental mean square displacement, which also

has been observed experimentally. If the Q-values become too large, so that the system's specific local properties come into play, the Rouse model starts to fail.

We have shown that this dynamic behavior continues to longer times if there are no constraints present in the system, i.e. the chains are short and do not entangle. If they are longer, the Rouse model starts to fail at longer times – longer than τ_e – when the mean square displacement of the segments reaches a special value. In the famous tube concept, this length scale is identified with the diameter of a virtual tube representing the topological constraints in the system. It has been illustrated that in the limit of very long polymer chains the tube model gives a perfect description of experimental data over the entire range of Q-values and Fourier times accessible by coherent NSE. The only parameter that has to be added to the Rouse parameters is the additional length scale in terms of the tube diameter. It has also been demonstrated by measuring the self-correlation function that the time dependence of the segmental mean square displacement changes due to the topological confinement. The observed behavior is in perfect agreement with the prediction of the reptation model if non-Gaussian behavior is taken into account.

In the intermediate regime of molecular weights, the chains are long enough to build entanglements but not so long that the tube concept gives a satisfactory description of the experimental data. At times longer than τ_e the single-chain dynamic structure factor does not show a fully developed plateau, but a slope that becomes more pronounced with decreasing molecular weight. This points to additional relaxation processes, which may be called secondary in the sense that they are additional to the main relaxation processes accounted for in the tube concept. The observation that they become more pronounced with decreasing chain length points to the fact that they have their origin in the finite length of the chains. Fluctuating chain ends can escape from the confinement by destroying the tube from both ends, a mechanism that is much more important than the creep process for intermediate chain length in the time regime of NSE. This CLF process explains the experimental observation that the plateaus at high Fourier times start to slope if the molecular weight decreases. The CLF process can be calculated and integrated into the reptation dynamic structure factor, giving an excellent description of experimental data over a wide range of Fourier times and Q-values (like before) and additionally for a wide range of molecular weights. Since the underlying process that causes finally CLF is still local reptation, there is no need to introduce new parameters. The tube diameter is still the only variable and it stays constant as expected within the reptation concept for all measured molecular weights if CLF is taken into account.

Finally, the fact that the tube is build by chains that have the same dynamics as the chain that is arrested in the tube leads to a finite lifetime of the tube

itself, and thereby to an additional "escape" mechanism, not by the test chain itself, but by a release of the confinement with increasing time. This CR effect can be accounted for in the calculation of the stress relaxation function as measured by rheology. However, though clearly observed in NSE experiments, a quantitative description of NSE data by a modified $S(Q, t)$ is still not available.

As mentioned in the introduction, the goal of polymer science is finally to clarify the relation between macroscopic properties and the architecture and composition of a polymer system. To reach this goal, all relaxation processes that are relevant for the macroscopic behavior have to be accessed, and the interaction between them has to be revealed. This could enable the production of "made-to-measure" polymer systems, i.e. with specific macroscopic properties by selectively manipulating the architecture and composition of the system.

It is evident that the experiments shown here are no more than a first step. A well-disposed reader may agree that the results presented give a more or less consistent picture of the dynamical behavior in polymer melts, though the quantitative provision for CR is not well developed. It is evident that the observed facts may serve as a basis for the understanding of more complicated architectures. The retraction mechanism of an arm that is part of a star polymer or of an H-shaped polymer may not be too different from the CLF mechanism. (Just regard the linear chain as a two-arm star). After the four arms of an H-polymer have retracted completely into the tube of the backbone, the creep of the polymer may be described with the same structure factor as the creep process of a linear chain, but with an unequal larger friction coefficient due to the relaxed arms, which serve as a kind of barb.

However, the dynamics of complicated architectures is more manifold compared to linear chains, the number of processes may be larger, and the interaction between them more complicated. Going one step further by mixing different architectures or mixing systems with different chemical structures results in a mixture of all these relaxation processes. The superposition and interaction of these relaxations follow rules that are up to now widely unknown. How does friction arise in a chemically heterogeneous environment? How can topological confinement of a chain be described if the tube is built by a blend that consists of two components with significantly different tube diameters?

Nevertheless, irrespective of how complicated a system may be, the opportunity remains to label small fragments of one component of such a system and thereby to manipulate the visibility of different processes for neutrons. In combination with the continuously growing opportunities in neutron scattering, chemistry, computing, and complementary experimental techniques

like NMR, dielectric spectroscopy or rheology, this may lead to significant progress in this field of research within the coming years.

References

Abdel-Goad, M., Pyckhout-Hintzen, W., Kahle, S., Allgaier, J., Richter, D., and Fetters, L. J., 2004, *Macromolecules* **37**, 8135.

Blanchard, A., 2004, *PhD thesis*, University of Münster.

Boothroyd, A. T., Rennie, A. R., and Boothroyd, C. B., 1991, *Europhys. Lett.* **15**(7), 715.

Clarke, N. and McLeish, T., 1993, *Macromolecules* **26**, 5264.

de Gennes, P.-G., 1981, *J. Phys. (Paris)* **42**, 735.

des Cloizeaux, J., 1990, *Macromolecules* **23**, 4678.

Doi, M. and Edwards, S. F., 1986, *The Theory of Polymer Dynamics*. Clarendon Press, Oxford.

Fatkullin, N. and Kimmich, R., 1995, *Phys. Rev. E* **52**(3), 3273.

Ferry, J., 1970, *Viscoelastic Properties of Polymers*. John Wiley & Sons, New York.

Fischer, E., Kimmich, R., Beginn, U., Moller, M., and Fatkullin, N., 1999, *Phys. Rev. E* **59**(4), 4079.

Flory, P., 1953, *Principles of Polymer Chemistry*. Cornell University Press, Ithaca, NY.

Gotro, J. T. and Graessley, W. W., 1984, *Macromolecules* **17**, 2767.

Graessley, W. W. and Struglinski, M. J., 1986, *Macromolecules* **19**, 1754.

Hsieh, H. L. and Quirk, R. P., 1996, *Anionic Polymerization: Principles and Practical Applications*. Marcel Dekker, New York.

Kamigaito, M., Ando, T., and Sawamoto, M., 2001, *Chem. Rev.* **101**, 3689.

Kirste, R., Kruse, W., and Schelten, J., 1973, *Makromol. Chem.* **162**, 299.

Likhtman, A. E. and McLeish, T. C. B., 2002, *Macromolecules* **35**, 6332.

Lodge, T. P., 1999, *Phys. Rev. Lett.* **83**, 3218.

Marshall, W. and Lovesey, S. W., 1971, *Theory of Thermal Neutron Scattering*, p. 65ff. Clarendon Press, Oxford.

Matyjaszewski, K. and Sawamoto, M., 1996, Controlled/living carbocationic polymerization, chap. 4 in *Cationic Polymerizations: Mechanisms, Synthesis, and Applications*, ed. K. Matyjaszewski. Marcel Dekker, New York.

McLeish, T. C. B., 2002, *Adv. Phys.* **51**, 1379.

Mezei, F., 1980, in *Neutron Spin Echo Proceedings*, Vol. 128, ed. F. Mezei, p. 3. Springer, Berlin.

Milner, S. and McLeish, T., 1998, *Phys. Rev. Lett.* **81**, 725.

Monkenbusch, M., Schaetzler, R., and Richter, D., 1997, *Nucl. Instrum. Meth. Phys. Res. A* **399**(2–3), 301.

Monkenbusch, M., Ohl, M., Richter, D., Pappas, C., Zsigmond, G., Lieutenant, K., and Mezei, F., 2005, *J. Neutron Res.* **13**, 63.

Montes, H., Monkenbusch, M., Willner, L., Rathgeber, S., Fetters, L., and Richter, D., 1999, *J. Chem. Phys.* **110**, 10188.

Odian, G., 1991, *Principles of Polymerization*, 3rd edn. John Wiley & Sons, New York.

Onogi, S., Masuda, T., and Kitagawa, K., 1970, *Macromolecules* **3**, 109.

Paul, W., Smith, G., Yoon, D., Farago, B., Rathgeber, S., Zirkel, A., Willner, L., and Richter, D., 1998, *Phys. Rev. Lett.* **80**(11), 2346.

Richter, D., Butera, R., Fetters, L., Huang, J., Farago, B., and Ewen, B., 1992, *Macromolecules* **25**, 6156.

Richter, D., Farago, B., Butera, R., Fetters, L., Huang, J., and Ewen, B., 1993, *Macromolecules* **26**, 795.

Richter, D., Willner, L., Zirkel, A., Farago, B., Fetters, L. J., and Huang, J., 1994, *Macromolecules* **27**, 7437.

Richter, D., Monkenbusch, M., Allgeier, J., Arbe, A., Colmenero, J., Farago, B., Bae, Y., and Faust, R., 1999, *J. Chem. Phys.* **111**, 6107.

Rubinstein, M. and Colby, R. H., 1988, *J. Chem. Phys.* **89**, 5291.

Schleger, P., Ehlers, G., Kollmar, A., Alefeld, B., Barthelemy, J., Casalta, H., Farago, B., Giraud, P., Hayes, C., Lartigue, C., Mezei, F., and Richter, D., 1999, *Physica B* **266**, 49.

Squires, G., 1978, *Introduction to the Theory of Thermal Neutron Scattering.* Cambridge University Press, Cambridge.

van Hove, L., 1954, *Phys. Rev.* **95**, 249.

Wischnewski, A., Monkenbusch, M., Willner, L., Richter, D., Likhtman, A., McLeish, T., and Farago, B., 2002, *Phys. Rev. Lett.* **8805**, 058301.

Wischnewski, A., Monkenbusch, M., Willner, L., Richter, D., and Kali, G., 2003, *Phys. Rev. Lett.* **90**, 058302.

Wischnewski, A., Zamponi, M., Monkenbusch, M., Willner, L., Pyckhout-Hintzen, W., Richter, D., Likhtman, A. E., McLeish, T. C. B., and Farago, B., 2004, *Physica B* **350**, 193.

Young, R. N., Quirk, R. P., and Fetters, L. J., 1984, *Adv. Polym. Sci.* **54**, 1.

Zamponi, M., 2004, *PhD thesis*, University of Münster.